Mixed-Mode Dynamic Crack Propagation using the Discontinuous Galerkin Method

A Thesis Presented for the
Master of Science
Degree
The University of Tennessee, Knoxville

Russell Thomas Hollman
May 2017

Copyright © 2017 by Russell Thomas Hollman
All rights reserved.

ACKNOWLEDGEMENTS

I would like to thank my advisor, Dr. Timothy Truster, who provided me with the amazing opportunity to work on his research team. Without his support, none of this would have been possible.

I would also like to thank Dr. Nicholas Wierschem and Dr. Dayakar Penumadu for being on my thesis committee and for providing me with their much-appreciated feedback.

Finally, I would like to thank my wife and parents who have supported and encouraged me throughout my entire college career.

ABSTRACT

A recently proposed Discontinuous Galerkin (DG) method for modeling nonlinear fracture mechanics problems in the context of the finite element method is investigated. The DG method provides a framework for fracture mechanics by employing interface elements within the region of interest where cracking is expected. Previous studies have shown that the use of traction-separation laws within the DG method have enhanced stability for dynamic problems by removing the issue of artificial compliance compared to intrinsic cohesive zone elements. The purpose of this thesis is to apply the DG method to a mixed-mode dynamic crack propagation problem, namely the Kalthoff-Winkler experiment. The Kalthoff-Winkler experiment is a benchmark dynamic fracture problem for predicting crack propagation in an impact-loaded prenotched plate. While this problem has been simulated using other numerical methods, the DG method has not yet been investigated in this mixed-mode dynamic context. Mesh sensitivity has been found in the case of intrinsic cohesive zone models; the inherent stability of the DG method in the dynamic context may lessen the degree of sensitivity. The DG method is applied to the Kalthoff-Winkler experiment using multiple meshes: structured and unstructured, linear and quadratic, coarse and refined, and the resultant crack paths from several simulations do not agree closely. An additional contribution of this thesis is a novel technique for visualizing cohesive element data through wireframe figures. The technique produces illustrations for visualizing zero-thickness interface elements as thin lines, upon which cohesive element data can be conveyed with color contouring. Possible explanations regarding the disagreement of simulated crack paths are suggested.

TABLE OF CONTENTS

LIST OF FIGURES

1. INTRODUCTION

In the past few decades, the field of fracture mechanics has developed into an established discipline of its own. Most universities with an engineering program now at least provide graduate level courses in the subject. While impossible to quantify, our understanding of how structures fail and our ability to prevent such failures has undoubtedly saved countless lives and prevented extensive property damage over the years. Interior and surface flaws are found in all metallic materials, not all of which are unstable under service conditions. In essence, fracture mechanics is the study of flaws to discover which are acceptably safe and which are liable to propagate as cracks, potentially resulting in the failure of the structure [1]. A. A. Griffith first pioneered fracture mechanics in 1921 after noticing a significant discrepancy between the stress needed to fracture bulk glass in the lab and the theoretical stress needed to break the atomic bonds. Griffith hypothesized that the lower experimental fracture strength of brittle materials could be attributed to the presence of microscopic flaws in the bulk material. After testing specimens with carefully assigned artificial flaws, he found that the product of the square root of the flaw length (a) and the stress at fracture (σ_f) was nearly constant, see Equation (1.1). Griffith later defined the constant using Young's Modulus (E) and the surface energy density of the material (γ), see Equation (1.2) [2]. Irwin [3] modified Griffith's theory to incorporate plasticity, observing that a plastic zone ahead of the crack tip dissipated energy as heat. Instead of just the surface energy term (γ), Irwin added a plastic dissipation term (G_p). Furthermore, Irwin defined the stress intensity factor (K) for calculating the available fracture energy in terms of the asymptotic stress and displacement fields at the crack tip.

$$\sigma_f\sqrt{a} \approx C \tag{1.1}$$

$$C = \sqrt{\frac{2E\gamma}{\pi}} \tag{1.2}$$

There are three basic types of loading that a crack can experience, as illustrated in Figure 1.1. Mode-I loading describes the state in which the principal load is applied normal to the crack plane, which tends to open the crack. Mode-II loading corresponds to in-plane shear loading, where the principal load is applied tangential to the crack plane, and tends to slide one crack face with respect to the other. Mode-III refers to out-of-plane shear [1]. Fracture mechanics failure analyses are, in principal, applicable to any loading mode (I, II, and III) as well as mixed-mode loading when more than one loading mode is present. In practice, however, the focus is on mode-I loading, which is usually justified since propagating cracks will quickly find local mode-I loading when presented with mixed-mode or pure mode-II loading. Standards and guidelines regarding the measurement of material failure properties and application of fracture mechanics concepts in design have been developed for mode-I loading only. Some researchers have considered in-plane shear (mode-II) and mixed-mode (mode-I/mode-II) loading to gain understanding of the fundamentals behind these types of failures. However, these investigators have primarily dealt with static loading conditions only. The underlying mechanisms that govern crack propagation behavior for mixed-mode dynamic problems have yet to be fully understood; little work has been done in this area [4]. One hypothesis is that crack growth follows the path that will maximize the energy release rate of the system, or in other words follow the path of

least resistance. Mode-I fracture requires the least amount of energy for crack growth, but if compressive stresses sufficiently restrict mode-I fracture, mode-II crack growth can be obtained [5].

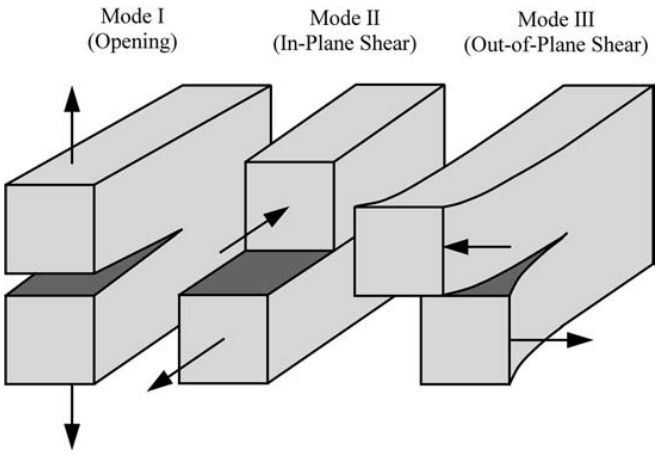

Figure 1.1 Three modes of crack loading [1].

The purpose of this thesis is to apply the recently proposed Discontinuous Galerkin (DG) method [6] to a mixed-mode dynamic crack propagation problem, namely the Kalthoff-Winkler experiment [7]. The Kalthoff-Winkler experiment, hereon referred to as the KW experiment, is a benchmark dynamic fracture problem for predicting the crack propagation in an impact-loaded prenotched plate. While this problem has been simulated using other numerical methods, the DG method has not yet been investigated in this mixed-mode dynamic context. This thesis will introduce some fundamentals of computational fracture modeling, introduce the DG method and formulation, and provide a literature review on the KW experiment and associated computational models before discussing the results of the new research in Chapter 6.

1.1 Finite Element Analysis & Newmark Integration

Finite Element Analysis is a powerful numerical technique for approximating solutions to field problems, which requires the determination of a spatial distribution of one or more dependent variables. It divides a larger problem into smaller, simpler parts known as finite elements. In each finite element, the field quantity is mathematically described by a simple spatial variation known as an assumed mode, or shape function. The finite elements are connected at points called nodes, at which the field quantity unknowns are solved for by a system of algebraic equations. The field quantity is approximated within the finite element by the nodal quantities and shape functions. The field quantity over the entire structure is approximated piecewise by the finite elements [8].

In dynamics, the equation of motion, which describes the behavior of the physical system in terms of its motion as a function of time, is described by the ordinary differential equation:

$$\mathbf{M}\ddot{\boldsymbol{d}} + \boldsymbol{C}\dot{\boldsymbol{d}} + \boldsymbol{K}\boldsymbol{d} = \boldsymbol{F} \tag{1.3}$$

where $\mathbf{M}$ is the mass matrix, $\mathbf{C}$ is the damping matrix, $\mathbf{K}$ is the stiffness matrix, $\mathbf{F}$ is the vector of applied forces, and $\mathbf{d}$, $\dot{\mathbf{d}}$, and $\ddot{\mathbf{d}}$ are the displacement, velocity, and acceleration vectors respectively. The numerical solution to the equation of motion is calculated by direct integration. Direct integration uses a step-by-step integration in time; behavior of the physical system is evaluated at separate instants separated by time increments Δt. Discretization in time is accomplished using finite difference approximations of time derivatives, for which many techniques have been developed [8].

One of the most widely used direct methods for solving the equation of motion is the Newmark family of methods [9], consisting of the following equations:

$$\mathbf{M}\mathbf{a}_{\mathbf{n+1}} + \mathbf{C}\mathbf{v}_{\mathbf{n+1}} + \mathbf{K}\mathbf{d}_{\mathbf{n+1}} = \mathbf{F}_{\mathbf{n+1}} \tag{1.4}$$

$$\mathbf{d}_{\mathbf{n+1}} = \mathbf{d}_{\mathbf{n}} + \Delta t\mathbf{v}_{\boldsymbol{n}} + \frac{\Delta t^2}{2}[(1-2\beta)\mathbf{a}_{\mathbf{n}} + 2\beta\mathbf{a}_{\mathbf{n+1}}] \tag{1.5}$$

$$\mathbf{v}_{\mathbf{n+1}} = \mathbf{v}_{\boldsymbol{n}} + \Delta t[(1-\gamma)\mathbf{a}_{\mathbf{n}} + \gamma\mathbf{a}_{\mathbf{n+1}}] \tag{1.6}$$

where $\mathbf{d}_{\mathbf{n}}$, $\mathbf{v}_{\boldsymbol{n}}$, and $\mathbf{a}_{\mathbf{n}}$ are the approximations of $\mathbf{d}(t_n)$, $\dot{\mathbf{d}}(t_n)$, and $\ddot{\mathbf{d}}(t_n)$ respectively. Equation (1.4) is simply the equation of motion in terms of the approximate solution, where (1.5) and (1.6) are finite difference formulas describing the evolution of the approximate solution with respect to time. The numerical parameters β and γ control characteristics of the algorithm, such as accuracy, stability, and the amount of algorithmic damping. In essence, equations (1.4-1.6) are three equations for solving the three unknowns $\mathbf{d}_{\mathbf{n+1}}$, $\mathbf{v}_{\mathbf{n+1}}$, and $\mathbf{a}_{\mathbf{n+1}}$, assuming $\mathbf{d}_{\mathbf{n}}$, $\mathbf{v}_{\boldsymbol{n}}$, and $\mathbf{a}_{\mathbf{n}}$ are known from the previous time step. Special cases exist within the Newmark family equations as the numerical parameters β and γ are changed.

One of the most well-known and widely used methods is the average acceleration method with $\beta = {}^1/_4$ and $\gamma = {}^1/_2$, which is the method implemented in this research. The average acceleration method provides second order accuracy and unconditional stability, meaning that stability does not impose a time step restriction in linear problems. Furthermore, this choice of numerical parameters provides algorithmic energy conservation with no algorithmic damping. There can also be different treatments of the mass matrix. Consistent mass matrices use the same shape functions to derive their coefficients as are used for the stiffness matrix; the mass is spatially distributed according to the shape functions. The simpler lumped mass matrices place mass at the nodes. A lumped mass matrix is diagonal, and a consistent mass matrix is not. There are many ways to distribute the mass in a lumped mass matrix, but this research used a row-sum technique for lumping [10]. Consistent mass matrices were used for all simulations in this thesis except for the one simulation using explicit integration, for which the lumped mass matrix is used. It should be noted that occasionally the time step was lowered to increase stability of the simulations, reducing the residual norm at the end of each time step; if a simulation blew up, the time step was lowered and the simulation rerun to provide better stability.

Numerical modeling has become an indispensable tool in the study of fracture mechanics since few practical problems have closed-form analytical solutions. One of the more recent methods is known as cohesive zone modeling, which can be easily implemented into existing

finite element codes. This method is discussed in the following section. Other existing methods for modeling fracture, such as the extended finite element method [11] and meshfree [12,14,13] methods, are discussed in Chapter 5.

1.2 Cohesive Zone Modeling

Cohesive zone modeling (CZM) is a popular class of computational methods used to model the complicated processes of dynamic fracture. CZM considers fracture as a gradual process of separation within small regions adjacent to the tip of a forming crack. The region ahead of the crack tip is known as the cohesive zone, which represents material that begins separating on an atomic scale. One of the difficulties in modeling crack propagation behavior is uncertainty of material behavior at this scale. Cohesive zone models attempt to provide a phenomenological solution to the problem through the use of traction-separation laws (TSLs). Dugdale [15] and Barenblatt [16] idealized the atomic separation as the separation of two surfaces coupled with a stress softening relation. The separation is resisted by tractions described by a phenomenological traction-separation law (TSL), thereby representing damage as a gradual degradation of cohesive tractions. The popularity of the method stems from the ease at which it is implemented into existing finite element codes by simply inserting interface elements along element edges. Using the interface elements, crack openings are represented as displacement jumps or discontinuities between neighboring solid elements. These crack openings are related to the interfacial stress at inter-element boundaries by the TSL [17].

Two classes of cohesive zone modeling have been proposed to date, differing in the assumed prefracture behavior of the interface elements. The intrinsic model assumes elastic behavior of interface element prior to fracture, whereas the extrinsic model assumes rigid behavior prior to fracture. Intrinsic cohesive laws assume that the cohesive traction has an initially elastic response until a critical stress is reached. Upon reaching the critical stress, the interfacial traction softens in correspondence with the TSL until it ultimately falls to zero and new free surfaces are formed as shown in Figure 1.2a. In contrast, the extrinsic cohesive laws assume that cohesive surfaces exhibit an initially rigid response without any separation prior to reaching the critical stress value. When the critical stress is met, interface elements are dynamically inserted into the mesh containing a prescribed extrinsic TSL as shown in Figure 1.2b.

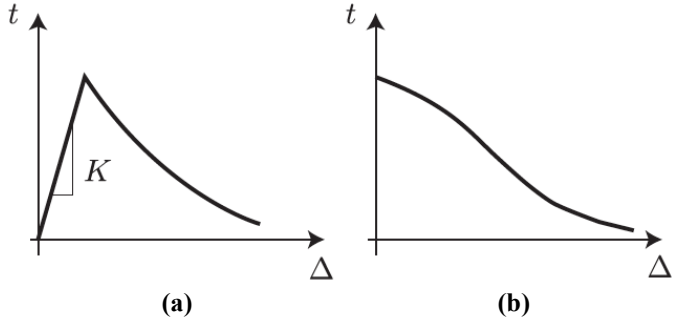

Figure 1.2 Traction-separation laws used in **(a)** the intrinsic approach and **(b)** the extrinsic approach [17].

These two basic classes of TSLs contain numerical issues that will be discussed in the next sections. The recently proposed Discontinuous Galerkin method aims to avoid the problems associated with the intrinsic and extrinsic methods. The DG method provides a promising alternative to traditional cohesive elements by allowing for discontinuous displacement jumps between bulk elements [17].

1.3 The Intrinsic Method

Intrinsic cohesive laws assume that the cohesive traction has an initially elastic response prior to reaching the critical stress, after which the traction decreases to zero and new surfaces are formed. One of the earliest intrinsic cohesive laws is the polynomial potential law developed by Needleman [18] to model delamination processes at material interfaces. This formulation consists of a polynomial representing a cohesive energy density and incorporates both normal and tangential separation at the material interface. Originally only normal separation was simulated, but Tvergaard [19] extended the law to allow for tangential failure. The next intrinsic traction separation law to come about was Needleman's exponential potential law [20]. In an attempt to be more grounded in physical principles, Needleman used the universal binding energy law for metallic interfaces and bulk metals wherein the cohesive energy density is represented with an exponential relationship.

The intrinsic cohesive zone models described above share the common feature of an initial elastic stiffness between the two sides of the interface. Because these elements consider the traction to be a single-valued function of the separation, this method requires that a finite separation always exist across the interface when a traction is applied. In other words, an intrinsic cohesive law assumes discontinuities in the displacement fields of the uncracked body from the start of the simulation. These initial separations are not present in the physical system, which is undamaged and thus does not contain any elements of reduced stiffness. These displacement jumps result in an artificial elasticity at the interelement boundaries, similar to adding springs between every element whose stiffness depends on the initial slope of the TSL. As a result, intrinsic cohesive elements alter the prefracture elastic response of the material. This artificial stiffness has serious implications in dynamic models because it can alter the speed and direction of propagating stress waves in the uncracked body. The effect of this numerical parameter must be calibrated such that the computed response closely matches results for meshes without cohesive elements. In particular, the initial stiffness of the cohesive law must be large enough for the artificial compliance to be minimized, but small enough to ensure that the problem converges. While increasing the initial slope of the cohesive law reduces the effects of artificial stiffness, it can severely restrict the time step. In order to maintain a stable formulation, a sufficient number of time steps must model the ascending branch of the TSL. Exceedingly high values of the initial stiffness can severely limit the time step and lead to excessively long computational times, but low values can exhibit severe artificial compliance effects. Finally, the intrinsic models, along with other cohesive element methods, possess the limitation that the crack path is constrained to nucleate and propagate only at the interelement boundaries. A possible remedy to lessen the impact of this mesh dependency is to employ highly refined meshes or adaptive schemes, which require large-scale simulations and parallel computing. [17].

1.4 The Extrinsic Method

Unlike the intrinsic method, the extrinsic method assumes an initially rigid response prior to debonding. The most widely used extrinsic cohesive law is the linear irreversible softening law initially proposed by Camacho et al. [21]. This TSL starts operating only after the specified failure criterion is met, upon which the extrinsic cohesive elements are dynamically inserted into the computational mesh. Because of the initially rigid response, adjacent continuum element boundaries remain coincident prior to fracture, thus eliminating premature finite separations and the issue of artificial compliance [17].

The primary disadvantage of the extrinsic method is scalability. As previously mentioned, interface elements are dynamically inserted into the computational mesh upon satisfaction of a specified fracture criterion. This, in turn, induces topological changes to the mesh, requiring the dynamic modification of mesh entities such as stiffness and connectivity matrices. This can prove to be computationally expensive in large-scale parallel simulations due to the need to restructure large sets of data throughout the calculation [17].

1.5 The Discontinuous Galerkin Method

The proposed Discontinuous Galerkin (DG) method takes some of the benefits from each of the methods and eliminates some of the larger issues associated with them. This method allows the user to insert cohesive interface elements in the initial mesh, thereby eliminating the need for dynamic insertion and the scalability problems that accompany it. Additionally, this method weakly enforces continuity across the interface prior to debonding, thus providing an initially rigid response and eliminating the issue of artificial compliance associated with intrinsic methods. Of particular interest in this thesis is the potential ability of the method to model arbitrary crack propagation in a dynamic context. However, the possible crack configurations are still limited by the topology of the finite element discretization, as in both the intrinsic and extrinsic approaches. Mesh sensitivity has been found in the case of intrinsic cohesive zone models, but the inherent stability of the DG method in the dynamic context may lessen its severity. In this thesis, the DG method will be compared to experimental results as well as other computational methods within the context of the Kalthoff-Winkler experiment.

The major sections of this thesis are as follows. The proposed Discontinuous Galerkin method is summarized in Chapter 2. A script for inserting the interface elements between the continuum elements is described in Chapter 3. A numerical verification of the dynamic algorithms of pertinent programs is provided in Chapter 4. A literature review on the KW experiment and associated models is provided in Chapter 5. And numerical simulations and relevant discussion is in Chapter 6; this chapter reports the results of the DG simulations and compares them to the results of two other methods: an intrinsic method [22] and a hybrid DG/extrinsic method [23]. Conclusions follow in Chapter 7 with some proposed areas for future work.

2. THE DISCONTINUOUS GALERKIN METHOD

2.1 Summary of the Formulation

The Discontinuous Galerkin (DG) method proposed by Truster and Masud [6] is used to model arbitrary crack propagation by adopting a Discontinuous Galerkin interface treatment embedded in a Continuous Galerkin formulation. The DG treatment is localized to the interelement boundaries while the Continuous Galerkin method is used in the bulk domains. The issue of artificial compliance associated with intrinsic methods is avoided by employing consistent numerical flux terms to weakly enforce continuity of the precracked displacement field. The progression from perfect adhesion to interface softening is handled seamlessly through the incorporation of an auxiliary field, which provides a smooth, easily simulated transition. Furthermore, the progression from interface softening to complete separation is handled without resorting to deletion of connectivities. The proposed method, while motivated by an augmented Lagrangian approach [24], also eliminates the need to add multiplier fields by instead using the average stress from the bulk domains as the measure of interface traction. This treatment results in a pure displacement method. A summary of the quasi-static formulation is presented below.

Consider an elastic domain $\Omega \subset \mathbb{R}^3$, containing two materials on either side of a bonded interface, Γ_{int}. The separation between the two materials, illustrated in Figure 2.1, is defined as $\boldsymbol{\delta} = [\![\mathbf{u}]\!] = \mathbf{u}^+ - \mathbf{u}^-$, where $\mathbf{u}$ is displacement and the + and – superscripts indicate the restriction of the field to the material on either side of the interface.

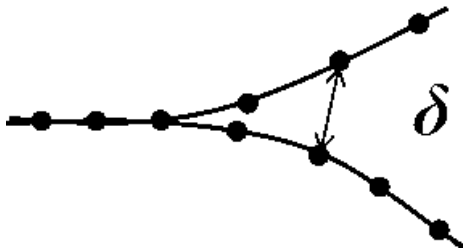

Figure 2.1 Separation gap across debonding interface [6].

Similar to typical elastoplastic finite element formulations, the separation gap $\boldsymbol{\delta}$ is tracked locally at the Guass points along the interface elements. The DG method differs from Lagrange multiplier methods in its treatment of the traction at the interface. Namely, the additional multiplier field associated with Lagrangian methods is replaced by the average traction $\{\boldsymbol{\sigma}\mathbf{n}\}$, henceforth referred to as the numerical flux, which is defined as:

$$\{\boldsymbol{\sigma}\mathbf{n}\} = [\gamma^+(\boldsymbol{\sigma}^+\mathbf{u}^+) + \gamma^-(\boldsymbol{\sigma}^-\mathbf{u}^-)]\mathbf{n} \tag{2.1}$$

where $\boldsymbol{\sigma}^+$ and $\boldsymbol{\sigma}^-$ are the restrictions of the stress tensors from the two materials onto the interface, Γ_{int}, and $\mathbf{n}$ is the unit outward normal to the interface. In the original formulation of the

DG method [6], the numerical flux is defined simply as the average of the stresses from each side of the interface. In this thesis, the definition has been extended to include the scalar weights γ^+ and γ^-, which are determined according to the procedure in [25]. This procedure relies heavily on the Variational Multiscale modeling approach to evaluate the numerical flux and stability parameters. The advantage of this procedure is that it does not require additional user-defined numerical tuning parameters. The procedure is particularly well suited for coupling materials with highly disparate moduli, such as composite materials [26]. This substitution of this numerical flux term changes the variational problem into a single primary field equation by incorporating information already known within the system, namely the stresses and displacements on either side of the interface, thus reducing the number of unknowns. The resulting functional is:

$$\begin{aligned}\mathcal{L}_{\mathrm{DG}}(\mathbf{u},\boldsymbol{\delta}) = {} & \mathrm{E}_{\mathrm{el}}(\mathbf{u}) + \mathrm{E}_{\mathrm{int}}(\boldsymbol{\delta}) - \mathrm{W}_{\mathrm{ext}}(\mathbf{u}) + \int_{\Gamma_{\mathrm{int}}} \{\boldsymbol{\sigma}\mathbf{n}\} \cdot (\llbracket \mathbf{u} \rrbracket - \boldsymbol{\delta}) \mathrm{d}\Gamma \\ & + \int_{\Gamma_{\mathrm{int}}} \frac{\mathrm{r}}{2} (\llbracket \mathbf{u} \rrbracket - \boldsymbol{\delta}) \cdot (\llbracket \mathbf{u} \rrbracket - \boldsymbol{\delta}) \mathrm{d}\Gamma \end{aligned} \tag{2.2}$$

where $\mathrm{E}_{\mathrm{el}}(\mathbf{u})$ is the elastic energy of the bulk materials Ω as a function of $\mathbf{u}$, $\mathrm{E}_{\mathrm{int}}(\boldsymbol{\delta})$ is the cohesive energy of the interface Γ_{int} as a function of $\boldsymbol{\delta}$, and $\mathrm{W}_{\mathrm{ext}}(\mathbf{u})$ is the external work done on the system as a function of $\mathbf{u}$. These energies make up the total potential energy of the system. The penalty parameter r becomes more critical for DG methods in order to ensure stability. By replacing the Lagrange multiplier and reducing the number of unknowns, traditional symmetric positive-definite solvers, which are used in most solid mechanics codes, are able to solve the discrete problem.

The weak form of the problem is obtained by taking the first variation of (2.2) with respect to the primary and auxiliary fields:

$$\begin{aligned} & \int_{\Omega/\Gamma_{\mathrm{int}}} \boldsymbol{\sigma}(\mathbf{u}) : \boldsymbol{\varepsilon}(\mathbf{w}) \mathrm{d}\Omega + \int_{\Gamma_{\mathrm{int}}} (\llbracket \mathbf{u} \rrbracket - \boldsymbol{\delta}) \cdot \{\boldsymbol{\sigma}(\mathbf{w})\mathbf{n}\} \mathrm{d}\Gamma \\ & + \int_{\Gamma_{\mathrm{int}}} [\{\boldsymbol{\sigma}(\mathbf{u})\mathbf{n}\} + \mathrm{r}(\llbracket \mathbf{u} \rrbracket - \boldsymbol{\delta})] \cdot \llbracket \mathbf{w} \rrbracket \mathrm{d}\Gamma = \mathrm{W}_{\mathrm{ext}}(\mathbf{w}) \qquad \forall \mathbf{w} \in \mathcal{V}_{\mathrm{w}} \end{aligned} \tag{2.3}$$

$$\int_{\Gamma_{\mathrm{int}}} [\mathbf{t} - \{\boldsymbol{\sigma}(\mathbf{u})\mathbf{n}\} - \mathrm{r}(\llbracket \mathbf{u} \rrbracket - \boldsymbol{\delta})] \cdot \boldsymbol{\gamma} \, \mathrm{d}\Gamma = 0 \qquad \forall \boldsymbol{\gamma} \in \mathcal{V}_{\gamma} \tag{2.4}$$

where $\mathcal{V}_{\mathrm{w}}$ and $\mathcal{V}_{\gamma}$ are the kinematically admissible spaces of weighting functions that satisfy the regularity requirements dictated by (2.3) and (2.4) respectively. Equation (2.3) weakly enforces bulk equilibrium and the condition $\llbracket \mathbf{u} \rrbracket = \boldsymbol{\delta}$, whereas equation (2.4) enforces the constitutive traction separation law for the interface. Assuming both materials are homogeneous and isotropic, the stress tensor is defined as:

$$\boldsymbol{\sigma}^{(\alpha)}\left(\mathbf{u}^{(\alpha)}\right) = \lambda^{(\alpha)} \mathrm{tr}\left[\boldsymbol{\varepsilon}^{(\alpha)}\left(\mathbf{u}^{(\alpha)}\right)\right]\mathbf{I} + 2\mu^{(\alpha)}\boldsymbol{\varepsilon}^{(\alpha)}\left(\mathbf{u}^{(\alpha)}\right) \tag{2.5}$$

with $\alpha = +/-$ in the same way it was denoted above. $\lambda^{(\alpha)}$ and $\mu^{(\alpha)}$ are the Láme parameters for each material on either side of the interface, and $\boldsymbol{\varepsilon}$ is the small strain tensor.

In order to solve the coupled system (2.3)-(2.4), the equilibrium equation (2.3) is discretized using solid finite elements and the constitutive equation (2.4) is enforced at the Gauss integration points along the interface Γ_{int}. This results in the traction at each Gauss point along the interface:

$$\mathbf{t}_{\text{g}} = \{\boldsymbol{\sigma}(\mathbf{u}_{\text{g}})\mathbf{n}\} + r(\llbracket \mathbf{u}_{\text{g}} \rrbracket - \boldsymbol{\delta}_{\text{g}}) \in \partial\Pi \tag{2.6}$$

where "g" denotes a specific Gauss point. With this traction, an implicit function for the interface separation $\boldsymbol{\delta}$ is defined in terms of the bulk domain quantities:

$$\boldsymbol{\delta}_{\text{g}} = \tilde{\boldsymbol{\delta}}(\llbracket \mathbf{u}_{\text{g}} \rrbracket, \{\boldsymbol{\sigma}(\mathbf{u}_{\text{g}})\mathbf{n}\}) \tag{2.7}$$

Substituting this equation, along with the discretized displacement fields $\mathbf{u}^{\text{h}}$ and $\mathbf{w}^{\text{h}}$, into the equilibrium equation (2.3) results in a nonlinear system of algebraic equations for the unknown displacement:

$$\begin{aligned}&\int_{\Omega/\Gamma_{\text{int}}} \boldsymbol{\sigma}(\mathbf{u}^{\text{h}}) : \boldsymbol{\varepsilon}(\mathbf{w}^{\text{h}})\text{d}\Omega + \int_{\Gamma_{\text{int}}} (\llbracket \mathbf{u}^{\text{h}} \rrbracket - \tilde{\boldsymbol{\delta}}) \cdot \{\boldsymbol{\sigma}(\mathbf{w}^{\text{h}})\mathbf{n}\}\text{d}\Gamma \\ &+ \int_{\Gamma_{\text{int}}} [\{\boldsymbol{\sigma}(\mathbf{u}^{\text{h}})\mathbf{n}\} + \text{r}(\llbracket \mathbf{u}^{\text{h}} \rrbracket - \tilde{\boldsymbol{\delta}})] \cdot \llbracket \mathbf{w}^{\text{h}} \rrbracket \text{d}\Gamma = \text{W}_{\text{ext}}(\mathbf{w}^{\text{h}}) \quad \forall \mathbf{w}^{\text{h}} \in \mathcal{V}_{\text{w}^{\text{h}}}\end{aligned} \tag{2.8}$$

The derivation of the DG method for elastodynamics mirrors that of the quasi-static formulation, with the exception of key assumptions relevant to dynamics. A full derivation by Truster and Masud can be found in [27]. The final form for dynamics using the Newmark time integration scheme [9], which ultimately incorporates the inertial terms, is expressed as:

$$\begin{aligned}&\textstyle\sum_{\alpha=1}^{2} \int_{\Omega^{(\alpha)}} \mathbf{w}^{(\alpha)} \cdot \frac{\rho^{(\alpha)}}{\beta \Delta t^2} \mathbf{u}_{\text{n+1}}^{(\alpha)} \text{d}\Omega + \textstyle\sum_{\alpha=1}^{2} \int_{\Omega^{(\alpha)}} \boldsymbol{\varepsilon}(\mathbf{w}^{(\alpha)}) : \mathbf{C} : \boldsymbol{\varepsilon}(\mathbf{u}_{\text{n+1}}^{(\alpha)}) \text{d}\Omega \\ &+ \int_{\Gamma_{\text{int}}} \llbracket \mathbf{w} \rrbracket \cdot \boldsymbol{\tau}_{\text{s}} \cdot (\llbracket \mathbf{u}_{\text{n+1}} \rrbracket - \zeta) \text{d}\Gamma - \int_{\Gamma_{\text{int}}} \{\mathbf{C} : \boldsymbol{\varepsilon}(\mathbf{w}) \cdot \mathbf{n}\} \cdot (\llbracket \mathbf{u}_{\text{n+1}} \rrbracket - \zeta) \text{d}\Gamma \\ &- \int_{\Gamma_{\text{int}}} \llbracket \mathbf{w} \rrbracket \cdot \{\mathbf{C} : \boldsymbol{\varepsilon}(\mathbf{u}_{\text{n+1}}) \cdot \mathbf{n}\} \text{d}\Gamma - \int_{\Gamma_{\text{int}}} \llbracket \mathbf{C} : \boldsymbol{\varepsilon}(\mathbf{w}) \cdot \mathbf{n} \rrbracket \cdot \boldsymbol{\delta}_{\text{s}} \cdot \llbracket \mathbf{C} : \boldsymbol{\varepsilon}(\mathbf{u}_{\text{n+1}}) \cdot \mathbf{n} \rrbracket \text{d}\Gamma \\ &= \textstyle\sum_{\alpha=1}^{2} \int_{\Omega^{(\alpha)}} \mathbf{w}^{(\alpha)} \cdot \left(\mathbf{b}_{\text{n+1}}^{(\alpha)} - \rho^{(\alpha)} \tilde{\mathbf{a}}_{\text{n+1}}^{(\alpha)}\right) \text{d}\Omega + \textstyle\sum_{\alpha=1}^{2} \int_{\Gamma_{\text{h}}^{(\alpha)}} \mathbf{w}^{(\alpha)} \cdot \mathbf{h}_{\text{n+1}}^{(\alpha)} \text{d}\Gamma\end{aligned} \tag{2.9}$$

where $\mathbf{b}$ is the body force, Γ_{h} is the Neumann boundary, ζ is the prescribed discontinuity related to contact problems, ρ is the mass density, $\mathbf{C} : \boldsymbol{\varepsilon}$ is the Cauchy stress, and $\boldsymbol{\tau}_{\text{s}}$ is the stabilization tensor accounting for geometry and material properties.

The distinguishing feature of the proposed DG method is that perfect adhesion is addressed without resorting to interelement springs or cohesive interface elements with a finite stiffness value. Particularly unique to this method are the numerical fluxes used to enforce interface constraints instead of adding extraneous variables such as the Lagrange multiplier. In other words, the displacement field $\mathbf{u}$ is weakly enforced to be in equilibrium with the interface gap $\boldsymbol{\delta}$ throughout the entirety of the numerical simulation. This treatment ensures the seamless progression from perfect adhesion to interface softening and complete separation, making the method more robust. Further discussion is contained in the reference [6].

2.2 Constitutive Model for Interface Behavior

The particular constitutive model used in this thesis is a generalization of the Talon-Curnier model [24,28], which is a bilinear function that allows for unequal limit states in shear and tension. A similar bilinear cohesive model is implemented by many other researchers using intrinsic cohesive zone methods and is discussed in Section 5.2. The Talon-Curnier constitutive model is illustrated in Figure 2.2 for the pure shear and tension cases, as well as the initiation criterion. Perfect adhesion is maintained below a specified critical stress σ_c followed by a linear softening relationship up to a critical gap δ_c, after which the interface is considered completely debonded and no traction forces exist between the two materials. Two models of unloading are explored in this thesis: residual unloading and elastic unloading. The generalized Talon-Curnier model assumes that the separation that has already taken place remains in the model, i.e. a residual gap is left unless the stress returns to zero and the interface crumples as illustrated in Figure 2.2a. An alternative to this model of unloading is to consider elastic unloading back to the origin, which will be discussed in Chapter 6. A proportionality factor β is incorporated into the model to allow for unequal critical values of tension and shear. Specifically, the proportionality factor scales the shear limits relative to the tension limits, as illustrated in Figure 2.2b [28].

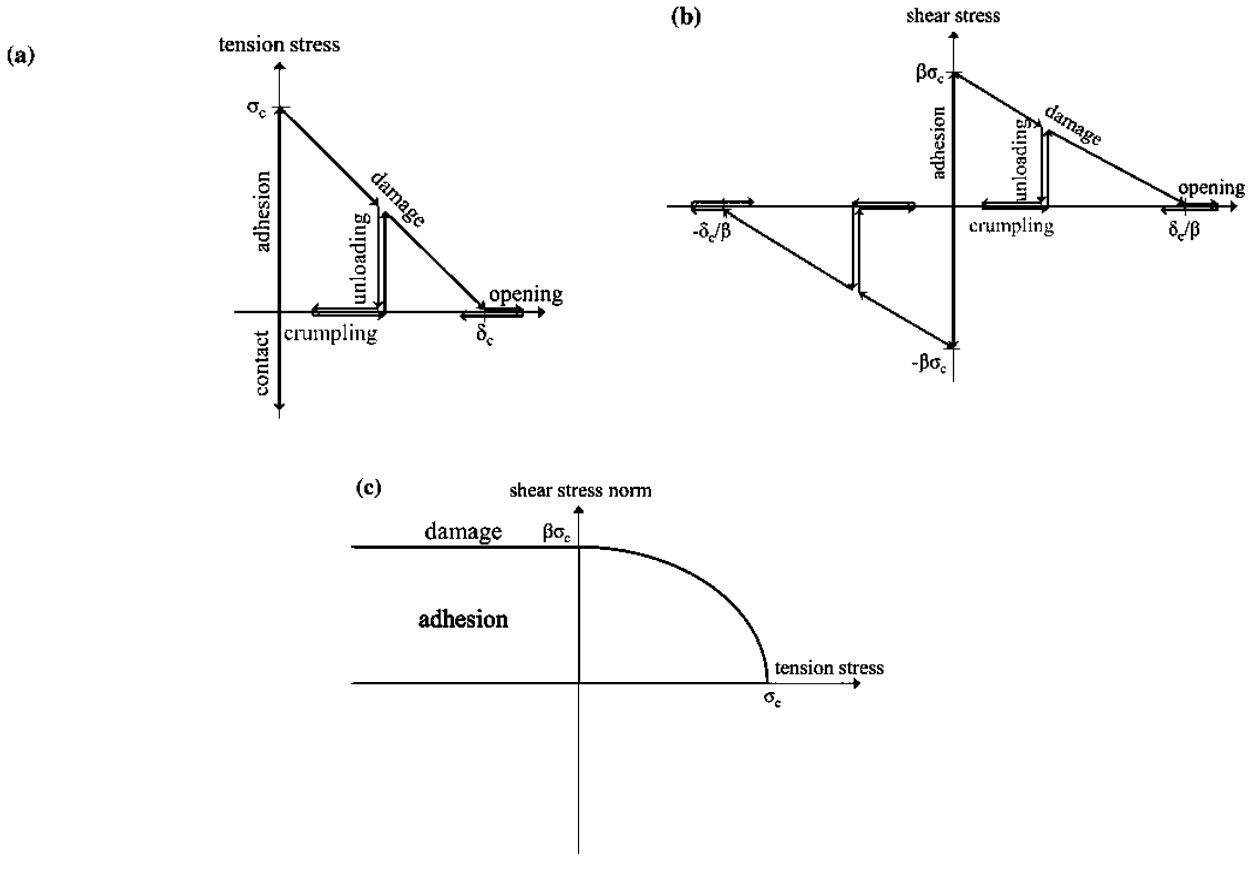

Figure 2.2 The generalized Talon-Curnier model for interface behavior for the **(a)** normal interaction **(b)** shear interaction and **(c)** initiation criterion [28].

Previous numerical studies applying the DG method to fiber composite systems have proven it to be a robust and viable option for numerical modeling alongside CZM approaches. The method accurately predicted fiber-matrix debonding when DG cohesive elements were localized to the fiber-matrix interface [6]. It also performed well when DG elements were inserted between all inter-element boundaries in the system to predict the behavior after significant interface failure [26].

3. DISCONTINUOUS ELEMENT INSERTION PROGRAM

The DG elements discussed in Chapter 2 are not widely available on popular finite element programs such as Abaqus. Therefore the implementation of the DG elements with regard to this research was performed in a research finite element code written in MATLAB. Furthermore, Abaqus does not provide a feature for inserting zero-thickness elements such as DG elements. Two free programs, developed by Truster [29] at the Computational Laboratory for the Mechanics of Interfaces (CLMI) at the University of Tennessee, were beta-tested and used to fulfill the requirements of this research. The Finite Element Analysis Program (FEA Program) is a companion linear finite element program capable of performing simulations using traditional intrinsic cohesive zone elements or DG elements. The Discontinuous Element Insertion Program (DEIP) is a set of MATLAB scripts for inserting zero-thickness interface elements into a continuous finite element mesh, and it was required to insert the DG elements for the simulations in Chapter 6. The program is capable of inserting zero-thickness elements between all bulk elements within a region, or along specific surfaces and interfaces, for both 2D and 3D problems. The source codes for these programs can be obtained for free online [29].

The creation of the DG meshes starts with Abaqus, where the preprocessing takes place, since the FEA Program does not contain a mesh generator. The geometry, material properties, loads, and boundary conditions are all created in Abaqus and stored in an input file. This input file is read into the DEI Program using a small script to extract the relevant information and store it in cell arrays within MATLAB. The program is then used to insert zero-thickness elements into predefined regions or subdomains. The insertion of new elements only employs topological operations on the original element connectivity of the mesh. It works by finding nodes along the specified interfaces and creating duplicates of them. Duplicated nodes are then assigned to the solid elements on the opposing side, thus creating an interface element between the two solid elements. This process is illustrated in Figure 3.1.

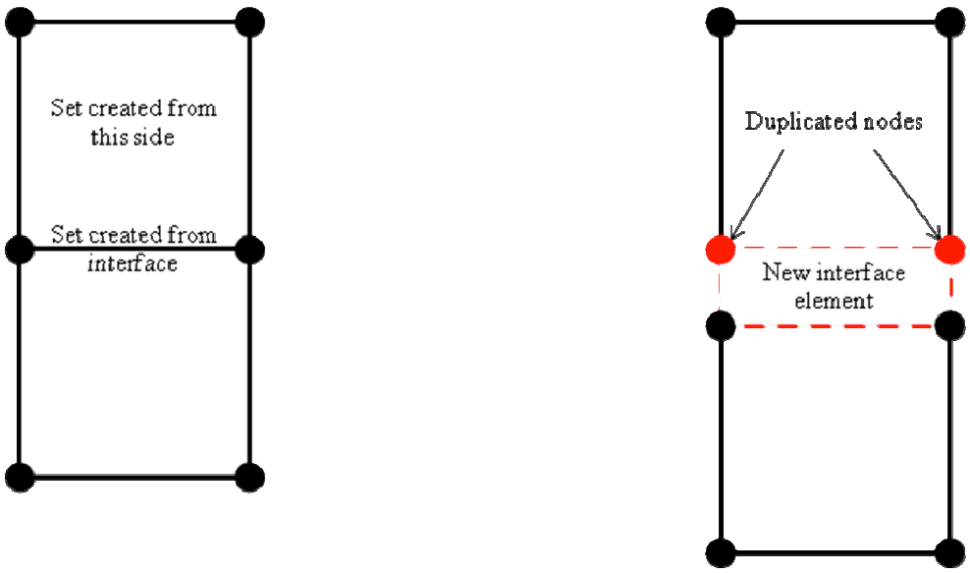

Figure 3.1 Interface element inserter schematic with separated interface for visual clarity [7].

Keep in mind that the DG elements are zero-thickness elements, which implies that the original geometry of the mesh is not affected. Duplicated nodes are placed in the exact location of existing nodes created in Abaqus. After the interface elements are created, the connectivity and node coordinate arrays are updated to include the new nodes and elements [26]. The numerical analysis is performed by the FEA Program using the input files created from the DEI Program, and typically involved parallel simulation using eight cores. Postprocessing and visualization of the output data was conducted in Paraview.

4. NUMERICAL VERIFICATION

The simulations performed for this thesis use a nonlinear finite element analysis program (NLFEA), the finite element analysis program (FEAP) discusses previously, and the commercially available Abaqus program. To ensure that the dynamics algorithms were the same in each program, a simple study was conducted in the context of a free vibration problem. The Abaqus manual is not clear on the specifics of its dynamics algorithms, and sometimes manuals do not correspond with actual codes. There are many time integration algorithms and element types, so it was important to obtain a node-by-node comparison to find out if each program uses the Newmark Method [9]. A free vibration problem was chosen because it maintains a constant total system energy over time; no energy is added or subtracted from the system by outside forces or boundary conditions. By using a problem with a constant system energy, any effects of algorithmic damping in the Abaqus calculations would be revealed in comparison to the FEA Program. Another nonlinear finite element analysis program (NLFEA Program), which can be run in MATLAB, was also used as a basis for comparison in this study [29]. The simulations run in the FEA and NLFEA Programs for this research use the Newmark average acceleration method for direct integration [9]. The numerical factors β and γ, which control characteristics of the algorithm such as accuracy, numerical stability, and algorithmic damping, were set as 0.25 and 0.50 respectively [8].

The example problem setup and mesh design are illustrated in Figure 4.1; units were not of importance and thus not included. The problem consisted of a solid rectangular 1.0 x 2.0 plate fixed on the left side and initially displaced $\delta = 0.001$ on the right side. Half of that displacement is imposed on the middle nodes. No y-direction initial displacement was prescribed to any of the nodes, but transverse vibrations appeared after the imposed displacements were released. A mesh of eight plane strain T3 elements was used, as illustrated, which have the same formulation in all three finite element codes. Only linear elements were investigated in this numerical verification since an Abaqus simulation was not conducted in this research (Abaqus does not provide a quadratic cohesive element). The initial displacement on the specimen was released and the plate was allowed to vibrate freely.

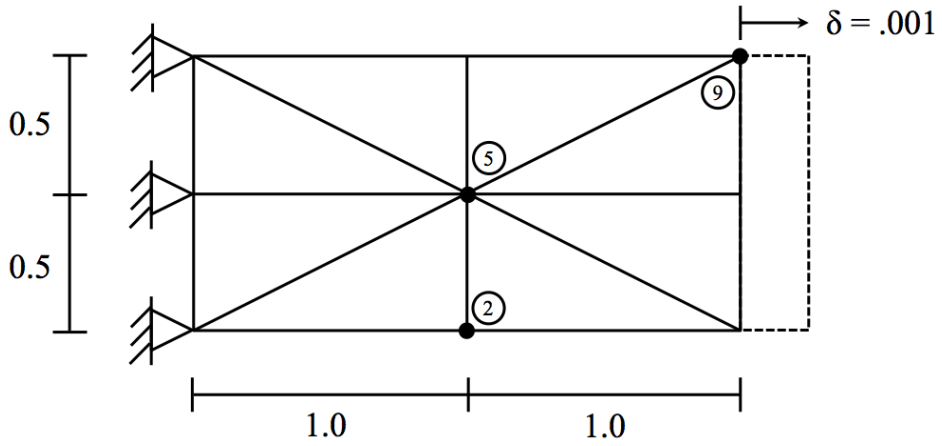

Figure 4.1 Numerical verification problem setup and mesh design: initial displacement, free vibration.

Material properties and dynamic simulation parameters were chosen to ensure that several oscillations were allowed to occur. The material properties are: $E = 1000$, $\nu = 0.25$, and $\rho = 0.03$. A time step of 0.01 was run 10 steps, resulting in a final simulation time of 0.1. The final horizontal displacements of the three representative nodes shown above were used as the metric for comparing the dynamic algorithms of the three analysis codes. The final displacements of nodes 2, 5, and 9 are given in Table 4.1.

Table 4.1 Horizontal displacements of nodes 2, 5, and 9 at the end of the numerical verification simulations.

	Node 2	Node 5	Node 9
FEA Program	5.64450000E-04	5.74840000E-04	8.51240000E-04
ABAQUS	5.64447255E-04	5.74844424E-04	8.51241639E-04
NLFEA Program	5.64447283E-04	5.74844452E-04	8.51241644E-04

The FEA Program only reported 5 significant digits, but the other two programs were exactly the same to 7 significant digits, which indicates that the three codes are using the same dynamic algorithms. This simple study signifies that the discrepancies between the FEA Program simulations and the Abaqus simulations were not caused by different treatment of the dynamics mathematics. As mentioned previously, the specific element type formulation was also the same in all three codes. However, it was discovered towards the end of this research that lower-order Abaqus elements, as used in the KW simulation, only employ lumped mass matrices; an option for editing this was not found. The KW simulations conducted in the FEA Program all used consistent mass matrices. Consistent mass matrices use the same shape functions as the element stiffness matrix to distribute mass across the element. Lumped matrices, on the other hand, distribute all mass to the nodes, resulting in a diagonal matrix. These two different treatments of mass distribution may account for the discrepancies between the Abaqus and FEA Program simulations for the KW problem. In conclusion, the three codes are the same at least for lumped mass matrix linear triangular elements. Now the different programs can be used to compare the DG method to other cohesive zone methods; then the differences can only be attributed to either the mass matrices, the stiffness matrices, or the physics of the interface elements.

5. IMPACT-LOADED PRENOTCHED PLATES

5.1 Early Studies

The focus of this thesis is on the application the recently proposed Discontinuous Galerkin (DG) method [6] to the Kalthoff-Winkler experiment, or the KW experiment [7]. In 1987, Kalthoff and Winkler developed a technique for subjecting cracks to almost pure mode-II conditions at extremely high rates of loading. The principle of the loading technique is shown in Figure 5.1. A plate specimen with two parallel edge notches is impact loaded by a cylindrical projectile between the two notches. The material used in their experiment was maraging steel type X2 NiCoMo 18 9 5, also know as 18Ni1900 or 18Ni(300), which is a super-high strength steel that also exhibits superior toughness [30].

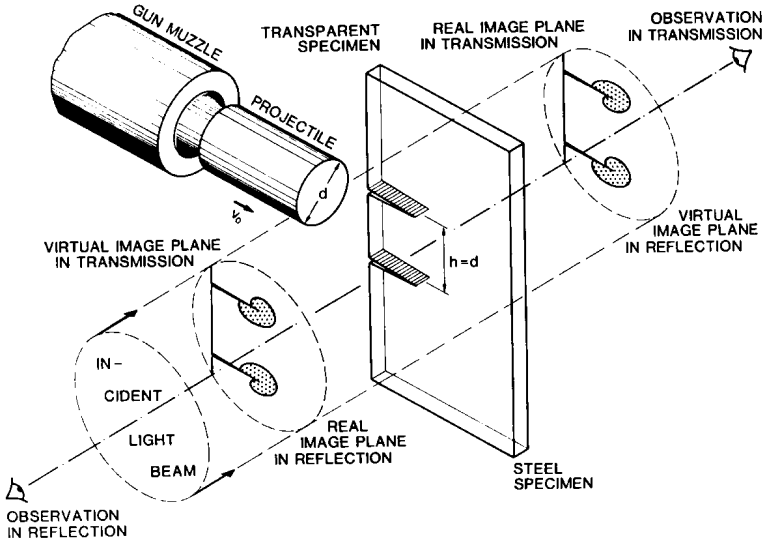

Figure 5.1 Technique developed by Kalthoff and Winkler for impact-loading a prenotched plate [4].

The researchers observed two different failure modes that were correlated to a parameter called the strain rate factor, which depends on the loading rate v_0 and notch radius r_0. By modifying the projectile speed and the acuity of the notch tip, two different failure modes were observed. At high impact velocities and high notch tip acuities, a shear band was formed ahead of the notch tip making an angle of about -10° with respect to the initial notch and arrested after propagating a short distance. For lower impact velocities and lower notch tip acuities, brittle fracture with a propagation angle of about 70° was observed to initiate from the notch tip and broke the specimen in two pieces. Above a critical speed, Kalthoff observed that the failure mode switched from a brittle 70° fracture to a ductile -10° shear band that arrested after a short distance despite the fact that energy provided by the higher speed projectile was higher (see Figure 5.3a). It should be noted that no specimens with a precracked notch tip (i.e. notch tip

radius equal to zero) exhibited the brittle 70° failure, only shear-band failure [7]. This thesis employs a mesh with a sharp notch tip radius ($r_0 = 0$), which would theoretically yield an infinite strain rate factor. However, the presence of cohesive elements requires a finite separation at the crack tip and eliminates the stress singularity. This thesis solely focuses on the brittle failure mode.

The brittle-to-ductile failure transition in these impact-loaded prenotched plates were very different from the behavior usually observed in quasi-static mode-I fracture [4]. Using the method of caustics, Kalthoff and Winkler were able to determine the mode of loading at the notch tip at discrete time intervals. They observed that the notch tip experienced a transition from mode-II loading to mode-I loading, after which mode-I loading controlled the inclined propagation of the crack tip. The impinging projectile initiated a compressive wave in the middle part of the specimen, generating a mode-II loading condition upon reaching the notch tip. The mode-II loading quickly transitioned to mode-I, upon which the crack opened and propagated at the 70° angle. These observations strongly describe a failure mechanism that is initially shear driven ultimately controlled by tensile stresses that propagate the crack at an inclined angle [7].

Three years later in 1990, Lee and Freund [31] analyzed an idealized impact-loaded prenotched plate using elastodynamic analysis. The problem analyzed by Lee and Freund was a semi-infinite plate with a single edge notch and an imposed velocity on one side of the crack, as shown in Figure 5.2. Their analysis showed that the 70° crack coincides with the direction of maximum circumferential tensile stress at the notch tip, indicating that the brittle failure of the KW experiments was driven primarily by mode-I loading in that direction. The analysis was conducted primarily to determine the time variation of the stress intensity factors at the notch tip, but another interesting result of the analysis was the revelation of a negative mode-I stress intensity in addition to the expected mode-II stress intensity. In mathematically small cracks, the presence of a negative mode-I stress intensity can indicate the interpenetration of the upper and lower surfaces of the crack [5]. In physical experiments, the surfaces on either side of the crack will exert contact forces on each other. To fix this non-physical phenomenon in numerical simulations, contact forces must be incorporated into the crack face boundary conditions, which can severely complicate the problem especially for modeling dynamic crack propagation along an arbitrary path.

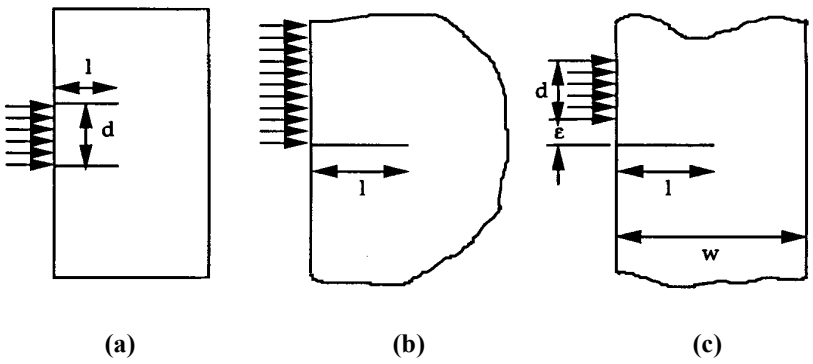

Figure 5.2 Impact-loading configuration for generating mixed-mode dynamic loading: **(a)** the 1987 Kalthoff-Winkler experimental **(b)** the 1990 elastodynamic analysis of a semi-infinite plate by Lee and Freund and **(c)** the 1995 Chandar experiment [5].

In 1994 Mason et. al. [32] confirmed this phenomenon experimentally using similar setup with C-300, another high-strength maraging steel. The experiments demonstrated contact between the two pre-crack faces as predicted by Lee and Freund. Mason et. al. also used specimens with only one notch instead of two. The difference allowed the researchers to observe the notch tip for a longer duration without interference from diffracting stress waves from a neighboring notch. Another interesting observation was the presence of both mode-II and mode-I failures in the same plate [32]. Recall that Kalthoff and Winkler reported that at low impact velocities a crack initiates from the notch tip and at high velocities a shear band initiates from the notch tip, as in Figure 5.3a. These two forms of failure do not occur simultaneously for any specimen [7]. On the other hand, Mason et. al. found that at intermediate impact velocities, a shear band initiates from the notch tip and arrests inside the specimen, after which a crack initiates from the tip of the arrested shear band (see Figure 5.3b).

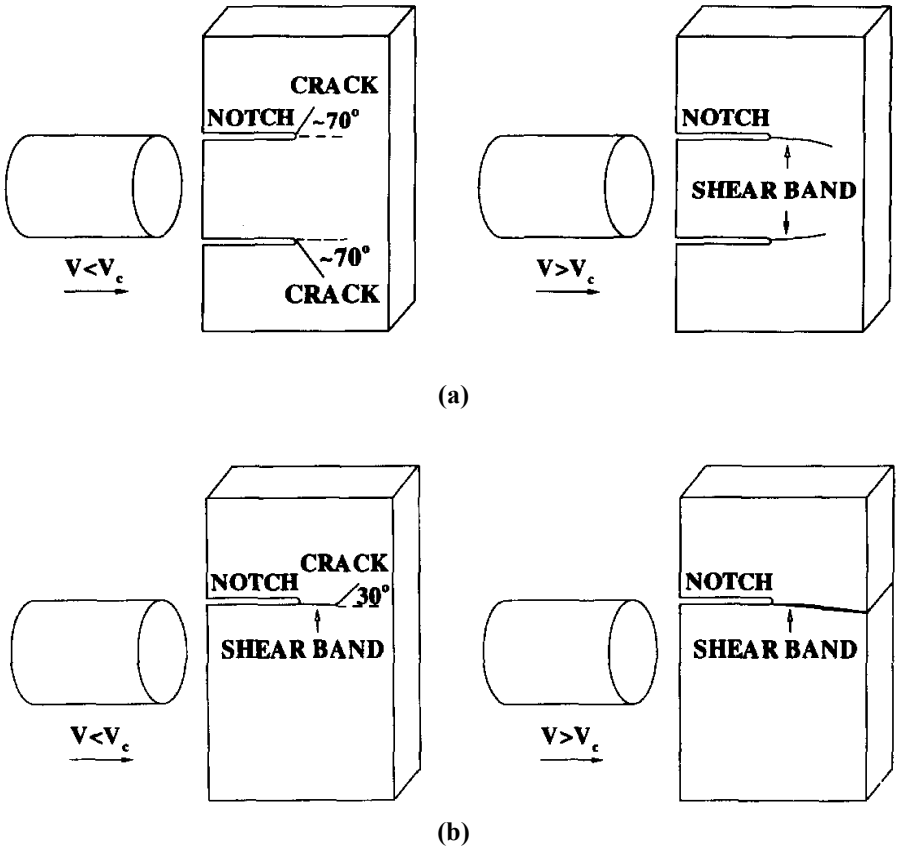

Figure 5.3 Failure modes observed by **(a)** Kalthoff and Winkler [7] and **(b)** Mason [32] and Zhou [34].

Needleman and Tvergaard conducted one of the first numerical studies of the KW experiment in 1995 [33]. Using finite element analysis, the team described the material behavior in terms of an elastic-viscoplastic constitutive model in a porous solid that accounts for ductile fracture by the nucleation and growth of voids. The focus was not on crack propagation, but on the initiation of failure and various parameters at the notch tip, such as stress and strain fields. Needleman and Tvergaard did not use the same material properties of the 18Ni(300) steel used in

the KW experiments, but instead used properties of a different but similar maraging steel. To simplify the model, the researchers took advantage of the symmetry of the plate and only modeled the top half, applying a boundary condition of $u_y = 0$ to the bottom of the new geometry. They assumed a notch width of 70 μm with a semicircular tip. To represent the projectile impact, a velocity boundary condition of 6.5 m/s and 16.5 m/s was applied to the face impacted by the projectile. The velocity was linearly ramped to these magnitudes over a rise time of 1 μs. A cross-quadrilateral mesh was employed where each quadrilateral was replaced by four crossed-triangle linear displacement elements, and local refinement at the notch tip was also utilized. Although thermo-mechanical properties were not reported in the KW experiments, Needleman and Tvergaard took thermal effects into account in order to test their theory that a thermo-mechanical mechanism was responsible for the brittle-ductile transition. They suggest that the transition is due to a greater increase in peak strain than peak stress with the increased loading rate provided by the higher projectile velocity. When strains at the crack tip become large enough, thermal softening ahead of the crack tip causes local deformation and initiates the shear band [33]. Needleman and Tvergaard's model provided one of the first idealizations of the KW experiments. Modeling half of the plate, representing the projectile with an applied velocity, and using cross-quadrilateral finite elements have been techniques used by many other researchers investigating the KW experiments.

That same year, Chandar [5] investigated failure mode transitions in polycarbonate plates with a single notch as seen in Figure 5.2c. Polycarbonate is a thermoplastic polymer that exhibits photoelastic effects, which allows for the observation of stress fields in the material. Polycarbonate also exhibits rate-dependent fracture mechanisms, as does the high-strength steel in the KW experiments and Mason experiments. Chandar obtained results similar to those of Kalthoff and Winkler's high-strength steel, where the failure mode transitions from brittle to ductile at high rates of loading [5].

In 1996, Belytshko and Tabbara [12] modeled the KW experiments, focusing specifically on the brittle failure mode. Belytschko and Tabbara used a meshfree Galerkin method, which is a meshless spatial approximation based solely on nodes. Most FEM use elements as the means of discretizing a model, hence creating a mesh. Meshfree methods use nodes/points to make up the shape functions, resulting in a grid of nodes. This approach can complicate the computational algorithms, particularly for numerical integration and parallel assembly. The growth of the crack in a meshfree method is modeled by extending its surfaces. The method uses least-squares interpolants for the trial functions, which require only a mesh of nodes and boundary descriptions to define. Since the method was intended for modeling crack growth, Belytshko and Tabbara focused solely on the brittle failure mode in the KW experiments, selecting a representative velocity of 16.5 m/s. Their results predicted crack angles originating from the notch tip at angles of 65-83°, similar to the results observed by Kalthoff and Winkler.

That same year, Zhou et. al. ran experiments [34] and computer simulations [35] on C-300 maraging steel and a titanium alloy, Ti-6Al-4V, using the single-notch configuration of Mason et. al. [32]. The Zhou-Rosakis-Ravichandran (ZRR) experiments have been described as a re-design to the KW experiments, with refined and improved experimental conditions for investigating shear-band failures [13]. For impact velocities above a critical value, a shear band propagates throughout the specimen. For impact velocities below this critical value, a shear band

propagates and arrests within the specimen, except for the C-300 steel specimen. In the steel specimen, a crack initiates from the shear-band tip at an angle to the shear-band propagation after the reflection of stress waves from the edge of the plate. The titanium specimen only exhibited shear-banding. While the failure mode transition is prompted by loading conditions, Zhou et. al. believed that the different behavior of the two materials suggested that the transition was also related to material properties. The researchers took real-time temperature histories along the shear-band paths using a high-speed infrared detector system. Temperatures in the shear band of the steel specimen reached 1400°C, 90% of its melting point, whereas temperatures in the titanium specimen only reached 450°C, about 30% of its melting point.

Coupled thermomechanical finite element simulations were also run for their experiments [35], taking into account finite deformations, inertia, heat conduction, thermal softening, strain hardening, and strain-rate hardening. The researchers used a prescribed velocity, ramped over 0.5 μs, similar to that of Needleman and Tvergaard [33]. In consideration of the separation of the projectile from the specimen, the velocity is applied for 47 μs, after which the surface is considered traction-free. Contact forces were applied on either side of the notch to prevent interpenetration. Critical strain criterion was used for the initiation of shear-banding, whereas critical stress criterion was used for the initiation of cracks. Their simulations accurately predicted shear band and crack propagation, shear-band speeds, and temperature measurements compared to experimental results. Additionally, the simulations captured the arrest of the shear band and initiation of the crack. The arrested shear band was first subjected to reverse shear upon reflection of stress waves from the edge of the plate, then mixed-mode loading ensues, eventually leading to a tensile failure at an angle of about 30° to the shear band.

In 1998 Zhou et. al. conducted another study on the growth of shear bands and failure mode transitions, comparing singly and doubly notched plate specimens [36]. Zhou et. al. recognized a discrepancy in the results reported by different researchers concerning failure mode transition in impact-loaded prenotched plates. Kalthoff and Winkler [7] observed either shear-banding or brittle fracture, but never simultaneously. Researchers such as Mason et. al. [32] and Zhou et. al. [34] reported crack initiation from the tip of an arrested shear band, both failure modes in one plate. Kalthoff and Winkler tested double notched specimens, while Mason et. al. and Zhou et. al. tested single notch specimens. Both studies used similar maraging steels, but they might have also had different thermal and mechanical properties contributed to their origin. Zhou et. al. [36] sought to reconcile these differences. Their approach was to test both plate configurations using the same C-300 maraging steel subject to identical heat treatments, making it possible to make direct comparisons and identify the factors contributing to the discrepancies. The plate geometries are shown on the next page in Figure 5.4.

Results for the single notch specimen are illustrated in Figure 5.3b, and results for the double notch specimen are illustrated in Figure 5.5. Clearly the results are very similar. Their experiments indicate that for the same material, plate geometries did not account for the discrepancy between the KW experiments [7] and those of Mason et. al. [32] and Zhou et. al. [34]. Their investigations show that the material is susceptible to both shear-banding and cracking. Furthermore, their investigations indicated that the different failure modes reported by

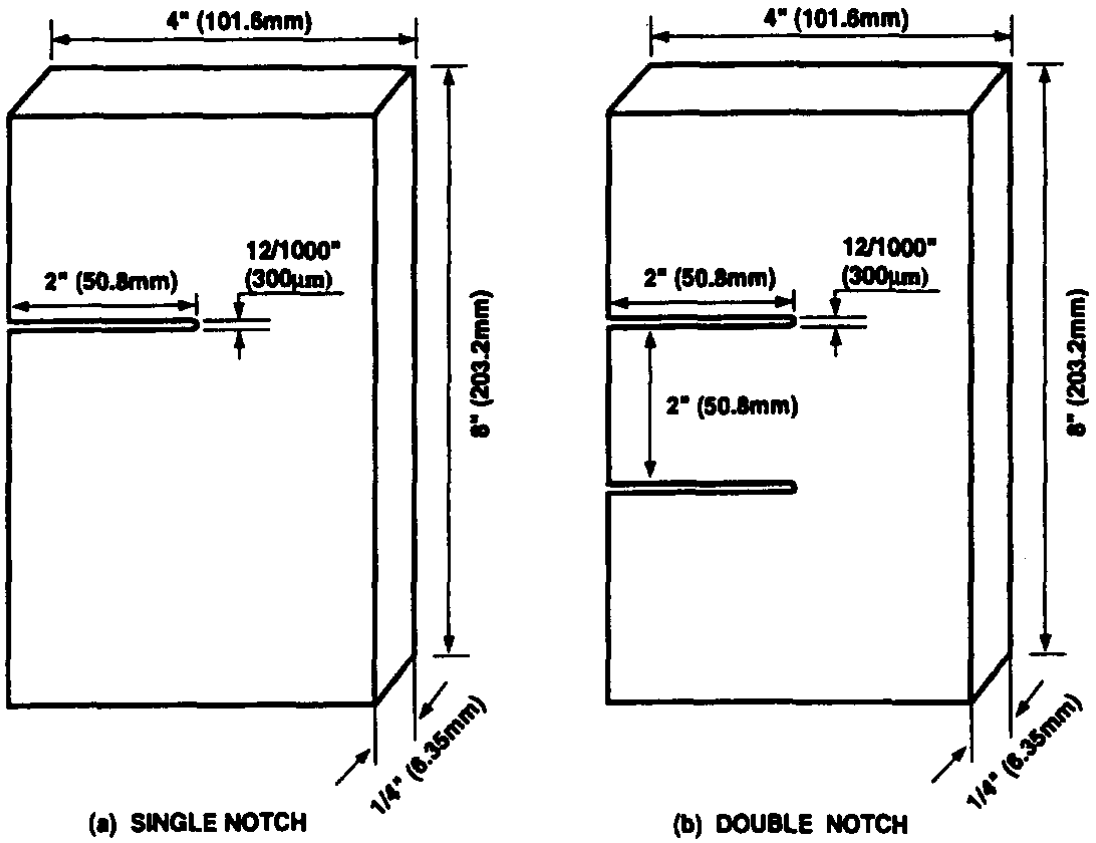

Figure 5.4 Single and double notch specimens used in Zhou et. al. [36].

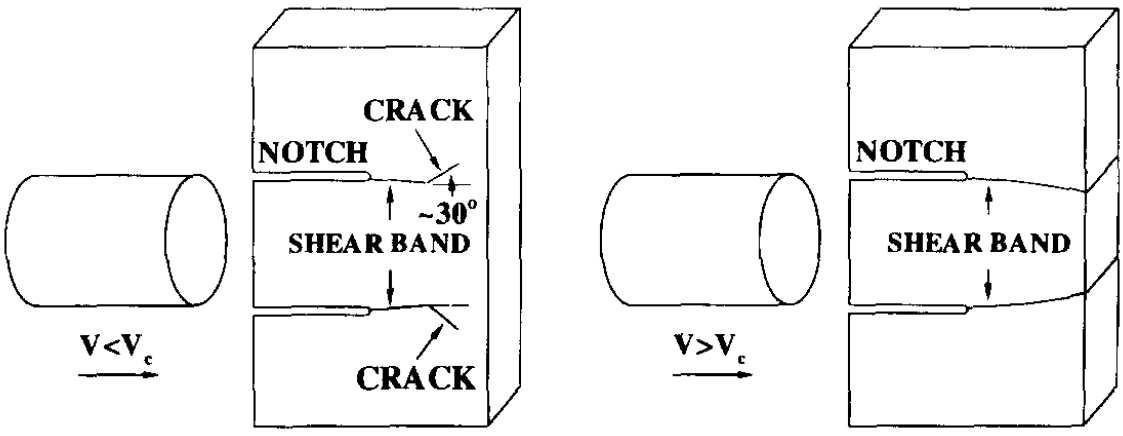

Figure 5.5 Failure modes observed in double notched specimens in the Zhou et. al. study [36].

Kalthoff and Winkler [7] were due to the fact that the maraging steel used in their experiments had a set of properties that were more susceptible to cracking at the notch tip at lower velocities. Their conclusion was that material properties play a primary role in dictating the mode of failure, not specimen geometry or configuration.

5.2 Recent Studies

Despite having more refined and updated experimental data, the KW experiment has prevailed as the problem of choice over the ZRR experiment in computational modeling of mixed-mode dynamic crack propagation, especially for modeling the brittle failure mode. Many researchers have used the benchmark KW problem as a context in which to test their numerical methods for modeling brittle crack propagation. The purpose of this thesis is to do just that: test the ability of the DG method to model mixed-mode dynamic crack growth. Not only does it require accurate dynamic solutions, which are made difficult by artificial compliance in intrinsic cohesive zone methods, but it requires the accurate prediction of crack propagation without predefining the crack path. The failure path is not specified a priori, which requires a computational method robust enough to model the crack initiation and direction of propagation. The DG method has proven to be more stable for dynamic problems than intrinsic CZM approaches by eliminating the issue of artificial compliance, and the inherent stability of the method suggested that it might be less sensitive to mesh topology.

Klein et. al. [14] simulated the KW problem in 2001 using meshfree methods with the internal virtual bond model, incorporating cohesive strength and finite work to fracture in the material description. Finite element interpolation is generally piecewise continuous, which inevitably results in dependence on local finite element edge orientation and discretization. Meshfree methods have the ability to minimize mesh sensitivity due to its interpolation scheme, not merely piecewise continuous but higher order continuous [13]. Klein et. al. [14] were only concerned with modeling the brittle fracture mode of failure, thus an impact velocity of 15 m/s was chosen. This method assumes crack extension occurs perpendicular to the direction of the maximum hoop stress around the crack tip. The crack velocity was assumed constant and crack branching was not considered. The advantage of cohesive modeling over this type of approach is that parameters such as crack speed and direction are outputs rather than inputs. The results depicted crack growth originating from the notch tip at an angle of 63°.

In 2002, Li et. al. [13] simulated the ZRR problem [34] in an attempt to accurately predict the phenomenon where an impact-loaded single notch plate presented both shear band and brittle fracture failure modes simultaneously, as discussed previously. The researchers did indeed simulate the failure mode transition using meshfree Galerkin methods with a thermo-elasto-viscoplastic constitutive model in both 2D and 3D. The results looked qualitatively similar to the behavior in Figure 5.3b.

The next year, Belytschko et. al. [11] simulated the KW problem using an extended finite element method (XFEM) based on a loss of hyperbolicity criterion. The XFEM approach, developed by Belytschko et. al. [37], extended the standard finite element method by enriching

the solution space for solutions to differential equations with discontinuous functions. Discontinuous basis functions were added to standard polynomial basis functions for nodes that belonged to elements with discontinuities, such as a crack. The method treated discontinuities, such as fracture, by switching from a continuum discontinuity to a discrete discontinuity when the governing partial differential equation lost hyperbolicity. A hyperbolicity indicator was defined as the minimum of the scalar projection of the acoustic tensor and was thus dependent on the stress and strain state in an element. The researchers treated the discrete discontinuity by using XFEM, thus allowing arbitrary discontinuities to be incorporated into the model without remeshing. A traction-separation law is imposed across the discrete discontinuity. Belytschko et. al. [11] established a standard of modeling the brittle failure mode in the KW problem that many researchers would later replicate in their simulations. Plate symmetry was used, reducing the model to half of the plate. A boundary condition of $u_y = 0$ was applied to the bottom face and a step velocity was applied to the face impacted by the projectile. The impact velocity was chosen as 16.5 m/s to attempt to reproduce the brittle failure mode. The material properties of maraging steel type 18Ni1900 were used: E = 190 GPa, $\nu = 0.3$, and $\rho = 8000$ kg/m^3. A 40 x 40 cross quadrilateral mesh was used with implicit-explicit time integration. The researchers obtained a nearly straight crack path originating from the notch tip at an angle of 58°, as depicted in Figure 5.6. Some damage also occurred in the bottom right of the plate, which was not reported by Kalthoff and Winkler [7]. As mentioned, the model used by Belytschko et. al. [11] has since been replicated by other researchers attempting to test the validity of their methods for predicting mixed-mode dynamic crack growth. The model assumptions, including geometry, boundary conditions, and treatment of the impact, have been accepted by many researchers as an acceptable technique for modeling the brittle failure mode witnessed in Kalthoff and Winkler's experiments. Three of these researchers will be discussed.

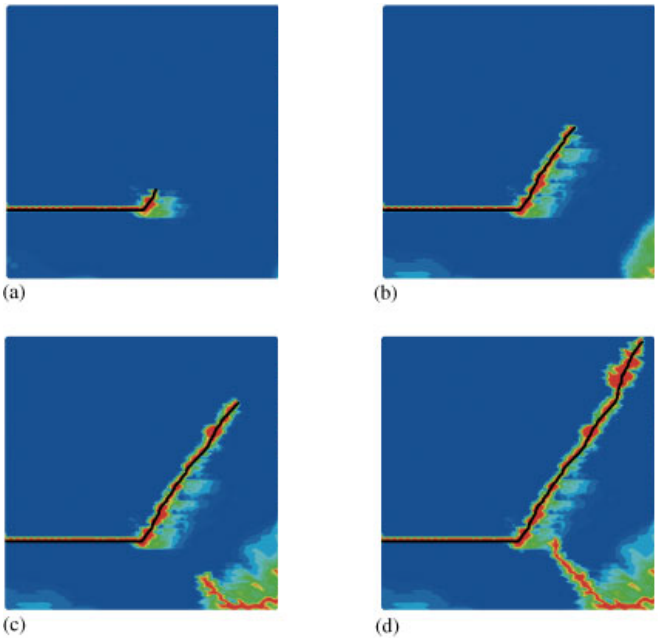

Figure 5.6 Crack evolution of Belytschko's KW simulation using XFEM with loss of hyperbolicity criterion at **(a)** t = 30.06 μs **(b)** t = 45.59 μs **(c)** t = 65.08 μs and **(d)** t = 85.57 μs [11].

In 2005, Zhang and Paulino [22] used an intrinsic cohesive zone method to investigate crack propagation in functionally graded materials. The researchers ran homogenous materials as well, including the KW experiment. Zhang and Paulino used a bilinear traction-separation law, allowing the users to more easily calibrate the initial stiffness necessary to minimize artificial compliance without becoming unstable. The TSL is illustrated in Figure 5.7. Zhang and Paulino adopted the model used in Belytschko's paper [11], with a fracture energy of 22.2 N/mm and cohesive strength of 1733 MPa. Several structured meshes composed of cross quadrilateral quadratic T6 elements of different sizes and aspect ratios were simulated. While most simulations in Chapter 6 of this thesis were conducted using linear T3 elements, one simulation was conducted using quadratic T6 elements, as did Zhang and Paulino. Although each mesh of Zhang and Paulino's possessed a different texture and/or level of refinement, all simulations predicted the same overall crack path angle of about 72° to 74°.

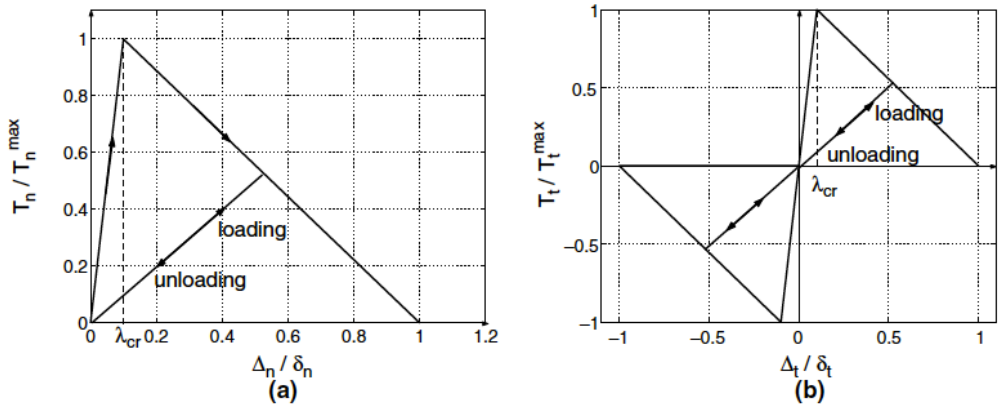

Figure 5.7 Bilinear cohesive model of interface behavior for the **(a)** normal interaction and **(b)** shear interaction [22].

In 2012, Park et. al. [38] simulated the KW problem using an extrinsic cohesive zone method with adaptive mesh refinement and coarsening (AMR&C). AMR&C was a technique developed by the researchers wherein the finite element mesh is altered during simulation. The crack tip region was adaptively refined, whereas the far field from the crack tip was adaptively coarsened. This approach was found to significantly reduce computational cost. Park et. al. used an extrinsic constitutive model know as the PPR model [39]. The Belytschko [11] standard for the KW problem was adopted for their simulations. Figure 5.8 displays the evolution of simulation conducted by Park et. al. [38]. The initial mesh topography was composed of a coarse 20 x 20 grid with local refinement around the notch tip, as illustrated in the top-left image in Figure 5.8. The researchers obtained a crack angle of about 62° originating from the notch tip.

In 2014, Nguyen [23] used a hybrid Discontinuous Galerkin/extrinsic cohesive zone method to simulate the KW problem. This hybrid method used a Discontinuous Galerkin formulation to model pre-fracture behavior and a standard extrinsic cohesive zone formulation to model post-fracture behavior. The pre-fracture treatment worked similarly to the DG method proposed by Truster and Masud [19] to eliminate the issue of artificial compliance. However, upon satisfaction of a failure criterion, the formulation switched to a traditional bilinear cohesive zone law. A fracture switch parameter β toggled between the two formulations. Adopting the

Belytschko standard [11], Nguyen obtained a crack angle of about 69° originating from the notch tip with an unstructured mesh of T3 elements. The results agreed well with the experiments, but the sharp transition from pre-fracture formulation to post-fracture formulation could potentially lead to instability in more complex problems. Particularly, Newton-Raphson algorithms might diverge when used to solve implicit dynamic problems with this formulation due to the non-smoothness of the system of equations [7].

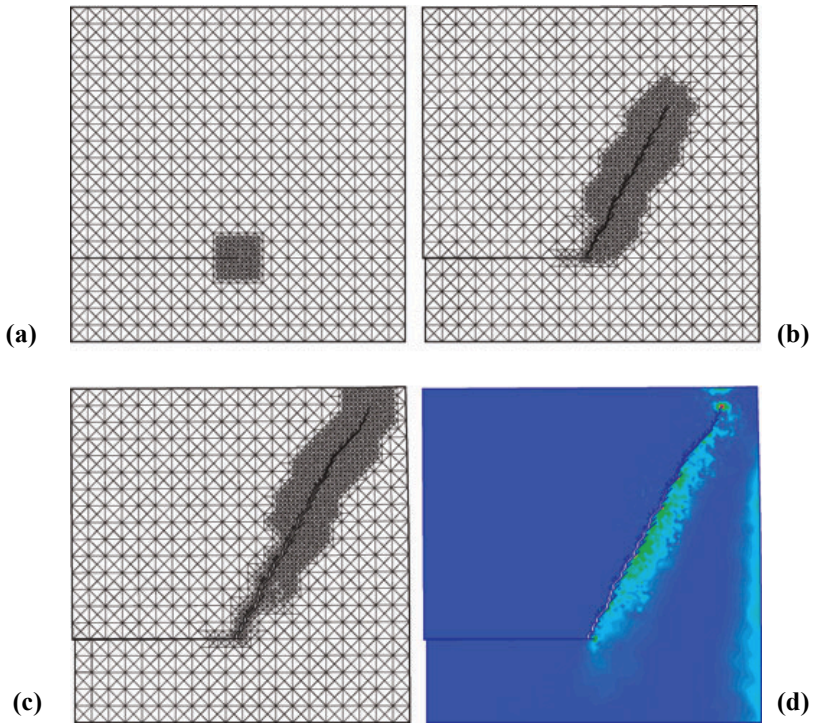

Figure 5.8 Crack evolution of Park's KW simulation using AMR&C with PPR constitutive model at **(a)** t = 0 μs **(b)** t = 55 μs and **(c)** t = 77.5 μs; **(d)** strain energy density at t = 77.5 μs [38].

The Kalthoff-Winkler simulation has become a benchmark problem in dynamic fracture modeling. While more recent experimental data has been reported on the shear-banding mode of failure [34], it appears little has been done experimentally regarding the brittle failure mode witnessed in the KW experiments. The purpose of this thesis is to test the ability of the DG method to model mixed-mode dynamic crack growth, thus the following simulations focus on the brittle failure mode, adopting the standard used by Belytschko [11] and others. The DG method is applied to the Kalthoff-Winkler experiment using structured and unstructured meshes, coarse and refined meshes, and linear and quadratic elements. The new simulations are primarily compared to the results the original experiment [7] of two other methods: Zhang's intrinsic bilinear cohesive zone model using quadratic elements [22] and Nguyen's hybrid Discontinuous Galerkin/extrinsic cohesive zone model using linear elements [23]. These two computational models of the problem are recent and closely match the results witnessed in the experiments for the brittle failure mode. Chapter 6 guides the reader through the DG simulations of the KW problem that were conducted for this thesis.

6. SIMULATING THE KALTHOFF-WINKLER EXPERIMENT

The process of running the DG simulations was fairly consistent throughout this research. First finite element models, including the mesh, geometry, boundary conditions, and loads, were created in Abaqus. The Abaqus input file was then run through the DEI Program in MATLAB to insert the interface elements and update connectivity and node coordinate arrays. After this preprocessing phase, the problem was analyzed in the FEA Program. Postprocessing and visualization was performed in Paraview, an open-source data analysis and visualization computer application. Paraview is capable of analyzing extremely large datasets produced by parallel computing, which was important in this research since simulations often required up to 10 cores to compute in a timely manner. An additional contribution of this thesis is a novel technique for visualizing cohesive element data through wireframe figures, which will be discussed in Chapter 6.

6.1 The Finite Element Model

Kalthoff and Winkler [7] investigated the failure behavior of impact-loaded prenotched plates, as discussed previously. The simplified numerical model, used by several of the researchers mentioned previously [12,36,14,11,22,38,23] is illustrated in Figure 6.1.

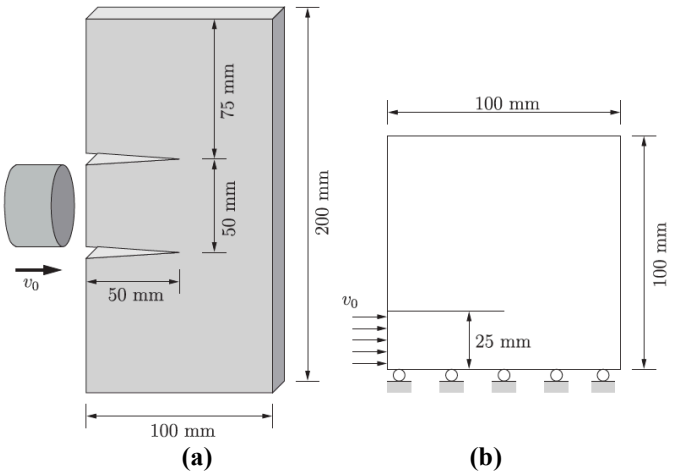

Figure 6.1 **(a)** Schematic of the Kalthoff-Winkler experiment and **(b)** the finite element approximation [38].

Zhang et al. [22] used an intrinsic method with a bilinear traction-separation law, as mentioned previously. This TSL allows the user to more easily calibrate the initial stiffness necessary to avoid artificial compliance without becoming unstable. The traction-separation law is illustrated in Figure 5.7. Several structured meshes composed of cross quadrilateral T6 elements of different sizes and aspect ratios were simulated. Although each mesh possessed a different texture and/or level of refinement, all simulations predicted the same overall crack path angle of about 72° to 74°. Also introduced previously, Nguyen [23] used a hybrid Discontinuous

Galerkin/extrinsic cohesive zone method to model the KW problem. Nguyen reported cracks originating from the notch tip at an angle of about 69° using an unstructured mesh.

The material for the Kalthoff-Winkler experiment was maraging steel 18Ni(300). It has a Young's modulus of 190 GPa, a Poisson ratio of 0.3, and a density of 8000 kg/m^3. Most simulations of the KW experiment prescribe a fracture energy of 22.2 N/mm and cohesive strength of 1733 MPa [11]. The material properties are conveniently tabulated below.

Table 6.1 The material parameters of maraging steel 18Ni(300) used in the simulation of the Kalthoff-Winkler experiment.

E (GPa)	υ	ρ (kg/m^3)	G_{Ic}/G_{IIc} (N/mm)	T_n^{max}/T_t^{max} (Mpa)	δ_n/δ_t (μm)
190	0.3	8000	22.2	1733	25.62

Due to the symmetry of the problem, only the upper half of the plate was modeled, as illustrated in Figure 6.1b. To ensure consistency with the physical system, a symmetry boundary condition was applied to the bottom edge of the model ($u_y = 0$). The projectile was assumed to have the same elastic impedance as the plate specimen, which implies that the impact velocity is one-half the projectile velocity. An instantaneous, constant impact velocity of 16.54 m/s was applied along the edge of the sample hit by the projectile by prescribing a displacement boundary condition of $u_x = v_0 \times t$ [23].

As previously mentioned, the major drawback of CZM approaches is that the crack path is confined to the topology of the finite element mesh. Crack tips are described by element corners, and the direction of crack propagation is limited to interelement boundaries. The crack path of the KW problem is not predefined, and in order to simulate arbitrary crack propagation, cohesive elements were placed in a large region where the crack was allowed to potentially grow. The crack grows in areas of high stress, where the local stress exceeds the maximum cohesive stress and causes the interface to lose its resistance to separation. The inherent stability of the proposed DG method suggested that it might be better able to predict this kind of crack growth compared to other cohesive zone methods. The goal of this thesis was to investigate this claim by applying the DG method to the KW problem and comparing the results to those from the original experiment and subsequent simulations by other computational researchers. The following section will reveal that the crack paths observed in the physical experiment, and reported in other papers, were not reproduced. The following section will also navigate through a series of simulations that were performed in an attempt to identify the source of the discrepancies between the differing solutions.

6.2 The Numerical Results

This research started with the two mesh topologies shown in Figure 6.2. The first mesh was a structured cross quadrilateral mesh laid out on an 80x80 square grid, which exactly matches the topology of a mesh tested in Zhang's research [22]. The second mesh was also a

structured cross quadrilateral mesh, but laid out on a 132x48 rectangular grid. This topology was chosen to provide element edges making an angle of about 70° to the horizontal while containing a similar number of elements as the 80x80 square mesh. The majority of the preprocessing took place in Abaqus where the geometry, discretization, material properties, loads, and boundary conditions were created. The plate geometries were discretized into their respective topologies with plain strain Q4 elements. A short MATLAB script was used to divide the Q4 elements into four T3 elements, creating the cross quadrilateral elements and meshes illustrated in Figure 6.2.

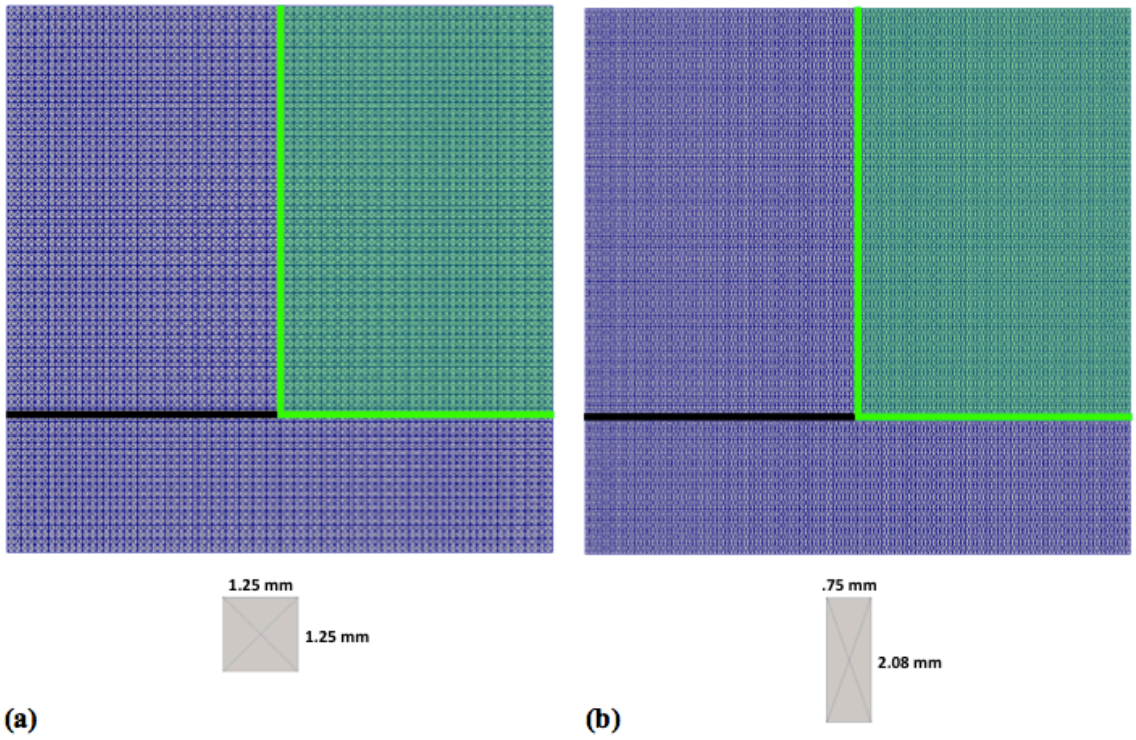

Figure 6.2 Mesh designs for the **(a)** 80x80 and **(b)** 132x48 discretizations. The green region and lines indicate the location of the DG interface elements, and the black line indicates the location of the notch.

This model was saved to an Abaqus input file, which was then read into the DEI Program introduced in Chapter 3. In this program the notch and DG interface elements were placed in the mesh, and the connectivity and node coordinate arrays were updated. The boundary condition array also needed to be manually updated to ensure that the impact load only applied to the elements below the notch. DG interface elements were placed along all interelement boundaries in the region shaded in Figure 6.2, as well as the vertical and horizontal edges initiating from the notch tip, as indicated by the green lines in the figure. It is unclear whether Zhang's meshes contained cohesive elements along the horizontal edge projected from the notch tip, an observation that will prove to be important in the next paragraphs. The total number of elements, bulk and cohesive, for the 80x80 and 132x48 meshes reached 40,000 and 39,600 respectively. Patch tests were also conducted for both meshes to check their ability to display a constant state of strain and both passed.

Both implicit and explicit integration schemes were applied to each mesh, with a time step of 20 ns for the implicit approach and 10 ns for the explicit approach. Provided the simulations remained stable, a sufficient number of time steps were used to obtain a total simulation time of 80 μs. The fracture paths for the two explicit simulations are shown in Figure 6.3 (top right region only, not the entire plate), and the fracture paths for the two implicit simulations are shown on the next page in Figures 6.4 and 6.5. Clearly the results from the physical experiment, and from simulations performed by other researchers, were not adequately reproduced. Namely, the diagonal cracks did not initiate from the notch tip. Instead, the plate experienced significant horizontal cracking before diverging in an inclined direction. This behavior suggests the influence of a strong, sustained mode-II loading with a transition to mode-I loading after the crack progressed horizontally for a significant distance. However, Kalthoff and Winkler's physical experiment showed that mode-II loading should quickly control the behavior at the notch tip after the compression wave rebounds, creating an inclined crack that initiates directly from the notch tip. The above simulations do not depict this immediate mode transition, but rather a delayed transition from mode-II to mode-I.

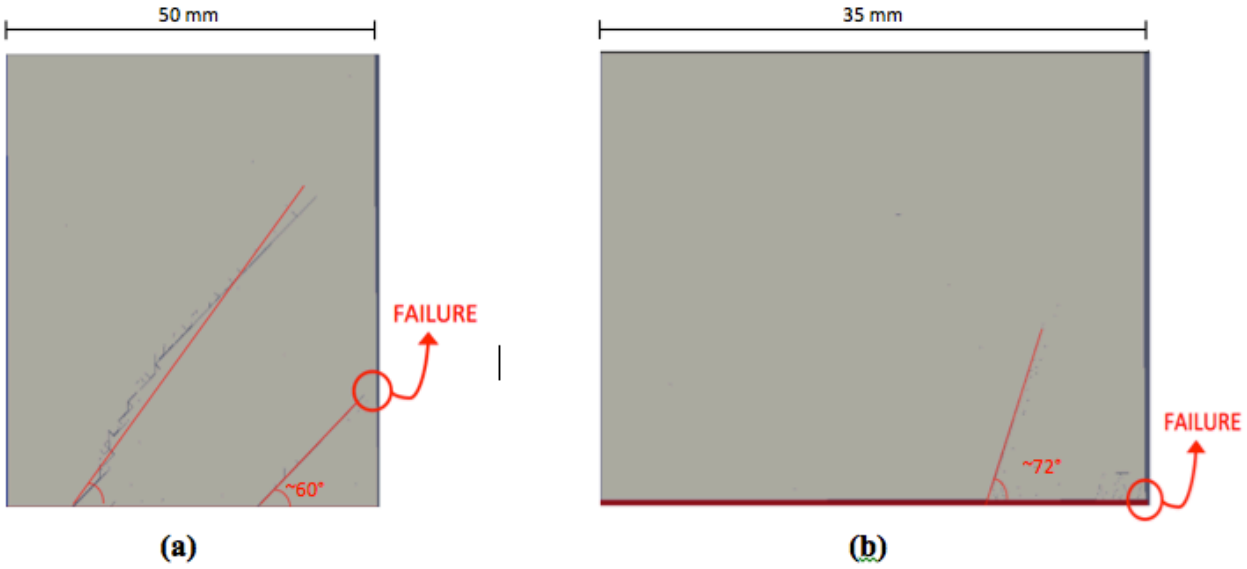

Figure 6.3 Fracture paths for the **(a)** 80x80 mesh and **(b)** 132x48 mesh using explicit integration (only top right region displayed, not entire plate).

Although the crack paths vary highly from the physical experiment and established research, the propagation angles seem feasible. Furthermore, the implicit crack configurations coincide well with their explicitly integrated counterparts. Figures 6.3a and 6.4 show that the 80x80 mesh propagated at an angle of about 60°, regardless of whether it was integrated implicitly or explicitly. Figures 6.3b and 6.5 show that the 132x48 mesh propagated at an angle of about 72° regardless of the method of integration. The crack angles were calculated by digitizing the path and imposing a linear trendline on the scatter plot. Since explicit integration requires a much smaller time step, which results in a longer computational time, and the results are similar for either method, this thesis employs implicit integration for the remainder of the simulations.

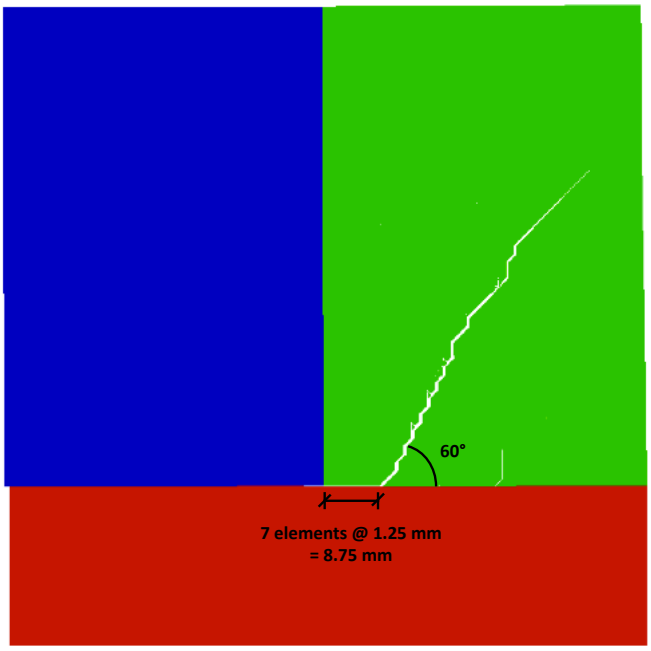

Figure 6.4 First fracture path for 80x80 mesh using implicit integration.

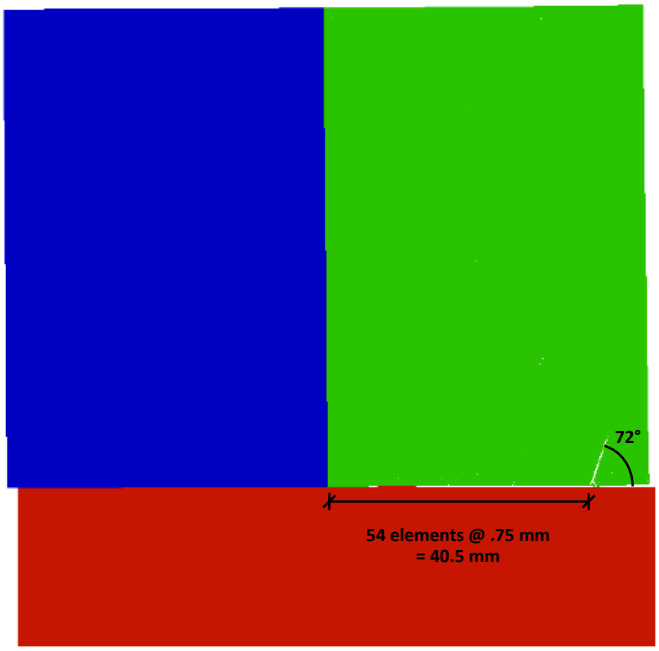

Figure 6.5 First fracture path for 132x48 mesh using implicit integration.

Figure 6.6 illustrates the severity of difference between the DG simulations and the simulations in [22]. Keep in mind that the 80x80 DG mesh above exactly matches the topology of Zhang's mesh below. However, Zhang's results closely resemble the results from the original experiment, where the crack grows at about a 70° angle originating from the notch tip.

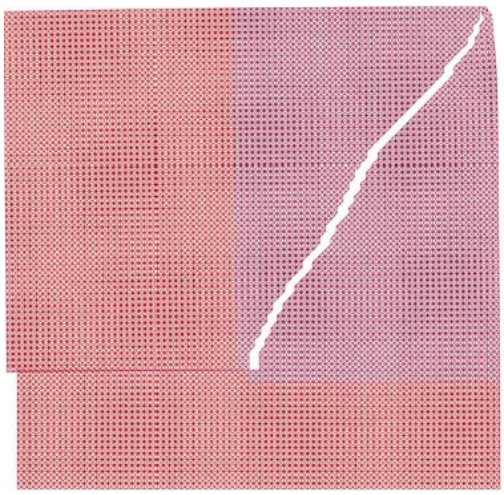

Figure 6.6 Fracture path of the 80x80 grid used in Zhang [22], which uses intrinsic cohesive zone elements. Notice that the initiation point of the path coincides with the notch tip, as expected from the experimental observations.

Previous implementations of the DG method strongly suggest that it is a viable option for numerical modeling relative to other cohesive zone methods [26,6]. The noticeable differences in the modeling of the KW experiment suggest that the error lie somewhere other than the mathematical formulation. In order to establish another basis for which to compare the DG examples, the 80x80 mesh was simulated in Abaqus using cohesive elements native to the commercial software. The Abaqus cohesive elements contain a standard bilinear intrinsic TSL. An initial stiffness of 6,764,164 N/mm^3 was prescribed, and it provided a stable simulation with minimal artificial compliance. This value was calculated in accordance with the recommendations in [22]. The crack path for the Abaqus simulation is shown in Figure 6.7.

This crack path also exhibits a horizontal tendency like the DG methods discussed previously. The Abaqus model predicts a relatively straight crack path initiating from a point 11.25 mm past the notch tip, growing at an incline of about 49°. Again, this simulation is not representative of the behavior in the experimental tests. Instead, the Abaqus-predicted crack configuration more closely resembles that of the DG simulations shown in Figures 6.3-6.5. In fact, the crack angles from the DG simulations are closer to the experimental results than the Abaqus simulation. The 80x80 DG model predicted a crack that initiated closer to the notch tip than the 80x80 Abaqus model, but at 40.5 mm the 132x48 DG model initiated the furthest away. The following paragraphs attempt to investigate the mechanisms behind these unexpected results.

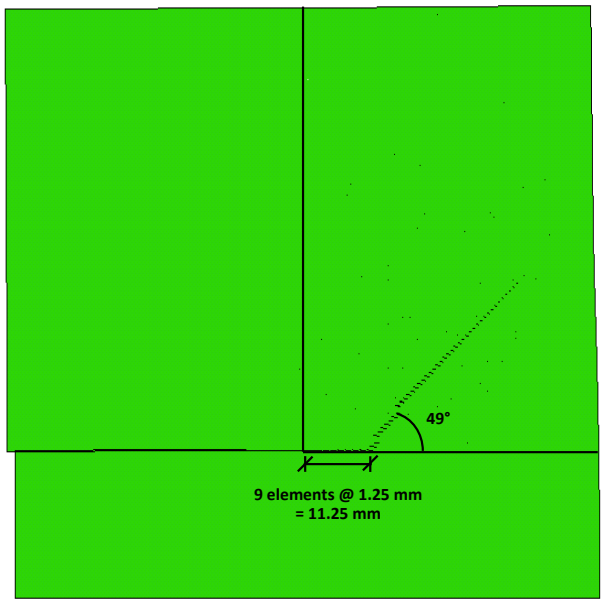

Figure 6.7 Fracture path of Abaqus 80x80 simulation using native intrinsic cohesive zone elements.

The first hypothesis was that the unloading behavior in the Talon-Curnier interface model (Figure 2.2) could be hampering the ability of the crack to diverge from the horizontal. Unlike the bilinear constitutive model, where traction and separation both decrease to zero resulting in linear unloading to the origin, the Talon-Curnier model has a traction that goes to zero while the separation remains finite at the maximum value until traction reaches zero. The Talon-Curnier model describes residual unloading whereas the bilinear model describes elastic unloading. The enlarged picture of the 132x48 implicit DG simulation in Figure 6.8a shows that minute cracks formed along every inclined element edge behind the growing horizontal crack, suggesting that the crack may have been trying to propagate at an incline but could not develop as quickly as the next horizontal edge could. Perhaps these residual cracks were building up and reducing the tensile resistance of the inclined edges directly above the horizontal, thus preventing the mode-I loading needed to cause the 70° diagonal crack. Figure 6.8b shows the stress field during this phenomenon and how a plume follows the horizontal crack but does not provide resistance right behind it. The elements directly above the horizontal are virtually unstressed.

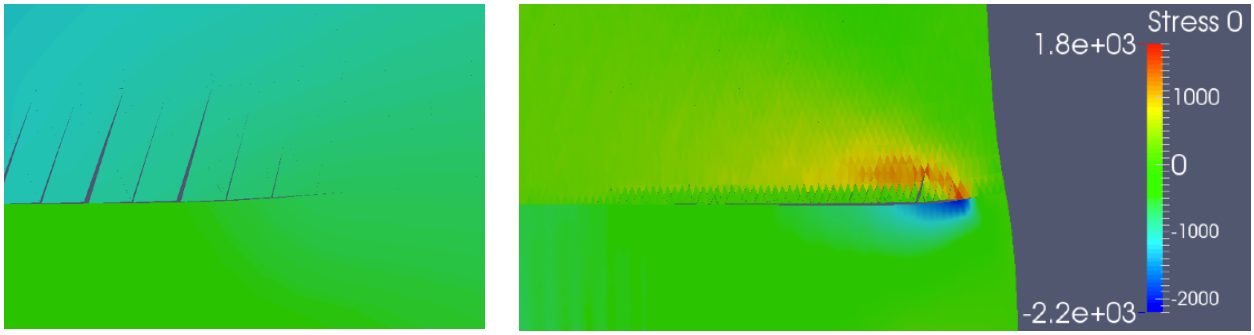

(a) **(b)**

Figure 6.8 **(a)** Image of the minute diagonal cracking following the primary horizontal crack and **(b)** image of the stress plume following the horizontal crack. Notice how minute diagonal cracking behind the primary horizontal crack reduces the resistance of material right above the horizontal ("Stress 0" is the stress in the x-direction in MPa).

To test this hypothesis, the unloading behavior of the cohesive elements was changed from a residual model to an elastic model. Instead of the Talon-Curnier interface model in Figure 2.2 where the interface separation is maintained until the stress returns to zero, an elastic model was used. The elastic model assumes unloading back to the origin, so the resistance of a damaged interface is stronger than in the residual model. In fact, elastic unloading was used for the remainder of the simulations in this thesis since the research from Zhang and Nguyen, as well as others, also use elastic unloading. The results for the 80x80 mesh and 132x48 mesh are shown in Figure 6.9. The simulations became unstable earlier in the fracture process, which is why only a short segment of the diagonal crack is shown.

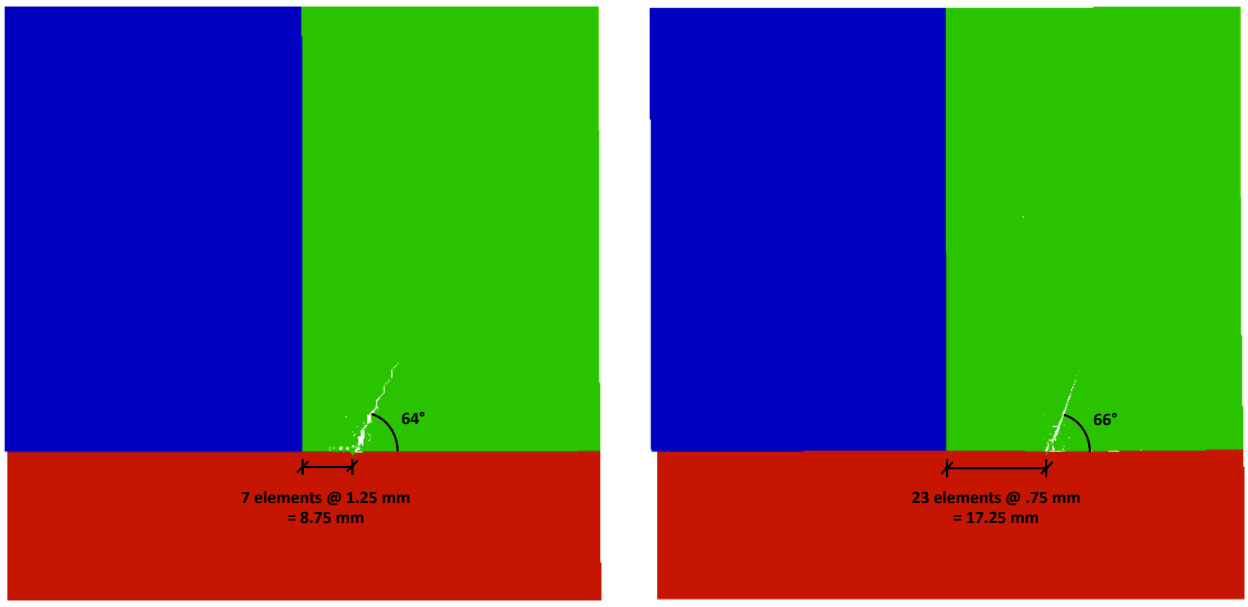

(a) **(b)**

Figure 6.9 Fracture path results using an elastic unloading model for **(a)** the 80x80 mesh and **(b)** the 132x48 mesh.

These results show improvement compared to the results for the residual unloading model (Figures 6.4 and 6.5). The 80x80 mesh predicts a crack angle of 64° compared to 60°, and the 132x48 mesh predicts diagonal crack initiation at 17.25 mm from the notch tip rather than 40.5 mm from the notch tip. These results show a closer match to the experimental observations of a 70° crack initiating from the notch tip. These results also show improvement in the crack angle compared to the value of 49° in the Abaqus simulation in Figure 6.7. Nonetheless, these simulations continue to predict cracks that do not originate from the notch tip. They also continue to show minute diagonal cracking behind the horizontal crack like in Figure 6.8. However, this cracking is less severe because of the unloading condition, which results in the improvements in Figure 6.9.

Ironically enough, Nguyen and other researchers had trouble with the crack propagating vertically from the notch tip before following a 70° angle [23,14]. Although the overall crack propagation formed an angle of about 69°, the initial crack propagation showed a short vertical segment along the interface projecting up from the notch tip [23]. The researchers investigated this phenomenon by removing the cohesive elements along this vertical edge. The result was very similar but without the initial vertical segment in the crack configuration. One might suggest using a similar approach for the simulations presented in this thesis by removing the cohesive elements along the horizontal edge projected from the notch tip. However, the goal of the DG method was to provide a robust technique capable of predicting natural behavior without significant user input. With this in mind, and considering the results shown in Figure 6.8, the vertical cohesive elements initiating from the notch tip were removed. The hope was to further limit the effects of the minute diagonal cracks that seemed to continue to prohibit a 70° crack from initiating from the notch tip. The results are shown in Figure 6.10.

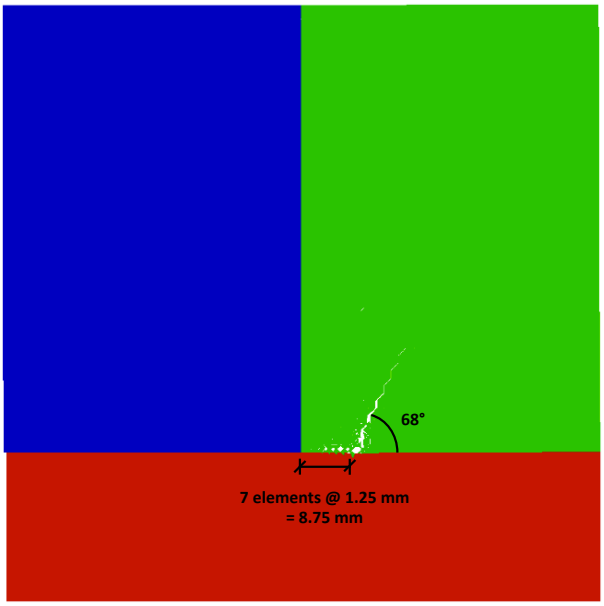

Figure 6.10 Fracture path for 80x80 mesh without cohesive elements in the vertical edge projecting from the notch tip (i.e. no cohesive elements between the blue and green regions).

The motivation behind this simulation also stems from the unique visuals developed specifically for this research. In order to better understand the cohesive elements themselves, a technique was developed for visualizing the cohesive elements without the bulk elements present. This technique provides valuable insight into the stress states of the cohesive elements, among other things. It produces wireframe illustrations, as shown in Figure 6.11, that provide a means of visualizing the zero-thickness interface elements as thin lines. Information such as the interface stress and separation, as well as the normal and tensile components of these vectors, can be visualized on these lines with color contouring. This allows the interface elements to be studied independently after a simulation is performed, and it provided valuable insights into the possible causes for the unexpected results encountered during this research.

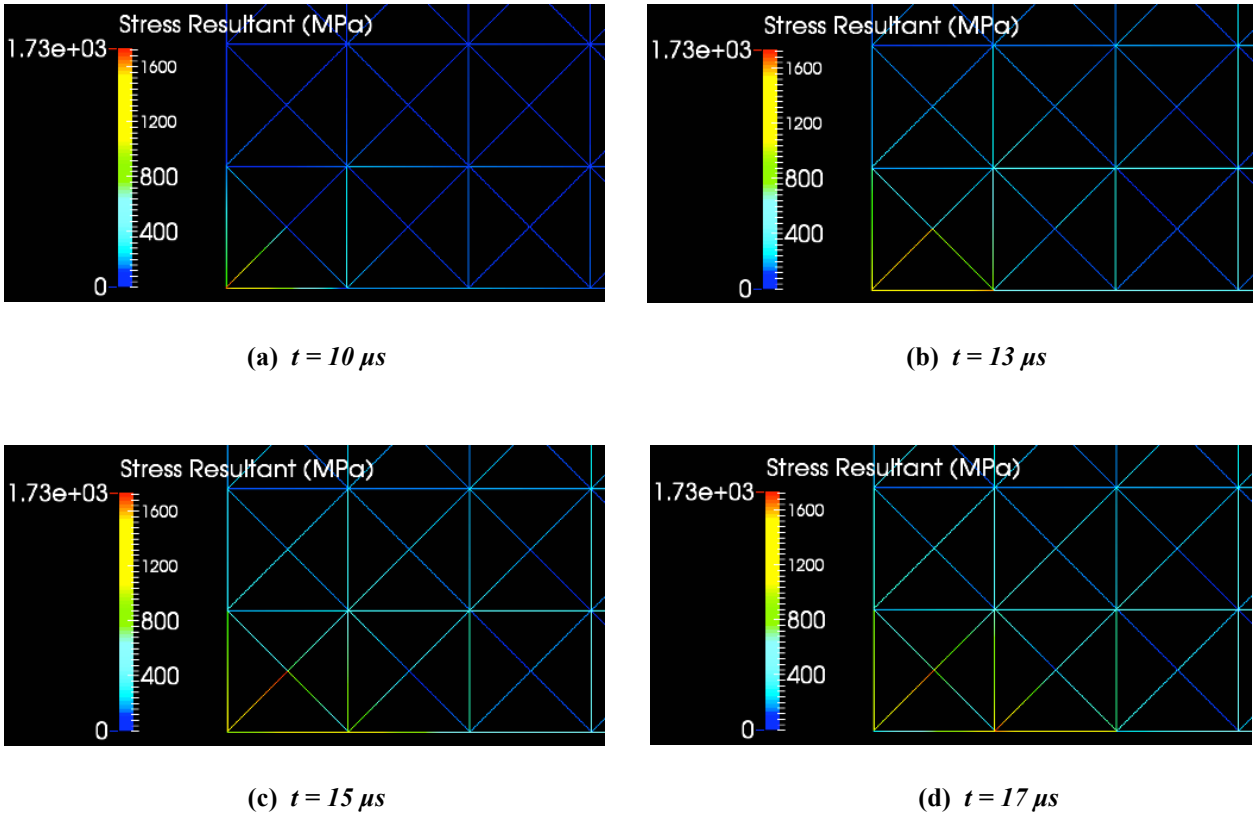

(a) ***t = 10 μs*** **(b)** ***t = 13 μs***

(c) ***t = 15 μs*** **(d)** ***t = 17 μs***

Figure 6.11 Stress resultant field ($\sigma_R = \sqrt{\sigma_n^2 + \sigma_t^2}$) of the DG elements near the notch tip, displayed on the wireframe figure for various time increments immediately after the compressive wave reaches the notch tip.

Figure 6.11 motivated the removal of the vertical interface elements because it revealed how the top left portion of the plate was not being fully engaged. When the vertical edge separates, stress cannot flow through it anymore. At 10 μs, a significant stress can be seen in the vertical cohesive element. Then at 13 and 15 μs, the stress can be seen to flow into the diagonal cohesive element. Finally at around 17 μs, the horizontal element cracks and proceeds to make its way across the plate. In order for the crack to propagate off of the horizontal at an incline, significant mode-I loading needs to occur on a diagonal or vertical cohesive element. Around 10 μs into the simulation, the vertical cohesive element begins to separate. If stress is trying to flow

into the “blue” region of the plate, it has to go around the vertical crack. So a sufficiently strong tension component, which is required for mode-I loading, cannot develop in the vertical or diagonal cohesive elements because the stress is flowing around them. By removing the vertical cohesive elements projecting from the notch tip, the “blue” region was better able to contribute to the development of a mode-I loading. However, the result in Figure 6.10 is only a slight improvement. The crack still initiated at 8.75 mm from the notch tip, but the 68° angle is more accurate than the 64° crack angle shown in Figure 6.9a.

As mentioned previously, the goal of the DG method was to provide a robust technique capable of predicting natural material behavior with minimal user input. The removal of targeted cohesive elements constitutes significant user input. An alternative possibility for facilitating stress flow into the left portion of the plate was mesh refinement. The hypothesis was that smaller elements may help develop mode-I loading on an inclined edge by shortening the distance for the stress to flow up and over the previously cracked vertical and diagonal edges. Additionally, mesh dependence of the arbitrary fracture pattern was assumed to decrease with increased refinement. Recall, the process zone is the area ahead of the crack tip where interface separation has occurred and the traction-separation law is operative. It is the region between where complete separation and no separation has occurred. Mesh refinement could improve the results of the experiment by providing a more accurate representation of this critical region.

To test this supposition, the problem was simulated using two refined meshes: a structured cross quadrilateral mesh with refinement around the notch tip, and an unstructured mesh with refinement around the notch tip. The mesh designs and resulting fracture paths are shown in Figures 6.12 through 6.14. The structured mesh contains 120,820 elements, bulk and cohesive, whereas the unstructured mesh contains 43,295; the refinement in the unstructured mesh is more locally prescribed. Clearly the structured mesh failed to produce the expected results, with virtually vertical crack angles originating from a point 12.27 mm from the notch tip. However, the unstructured mesh provided the most accurate crack configuration of any of the simulations, with a 74° crack angle originating from the notch tip. Zoomed-in images of the mesh design around the crack tip in Figure 6.14 show the most significant difference between the two designs. Notice how the unstructured mesh does not have cohesive elements extending horizontally from the notch tip, therefore eliminating the possibility of horizontal crack propagation from the notch tip. Furthermore, the region where cohesive elements are located extends to the bottom of the plate, encompassing all material right of the notch tip.

As previously discussed, Nguyen et al. [23] simulated the Kalthoff-Winkler using an unstructured mesh with local refinement around the notch tip, but their results showed a crack angle of 69° initiating from the notch tip. Their mesh contained elements as small as 0.25 mm, which closely matched the size of the refined meshes above. Although their mesh was unstructured, they had horizontal and vertical edges projecting out from the notch tip. It is clear that cohesive elements were inserted along the vertical face because the researchers removed the vertical edge after their crack configuration followed is for a short segment. However, it is unclear whether the researchers inserted cohesive elements along the horizontal edge.

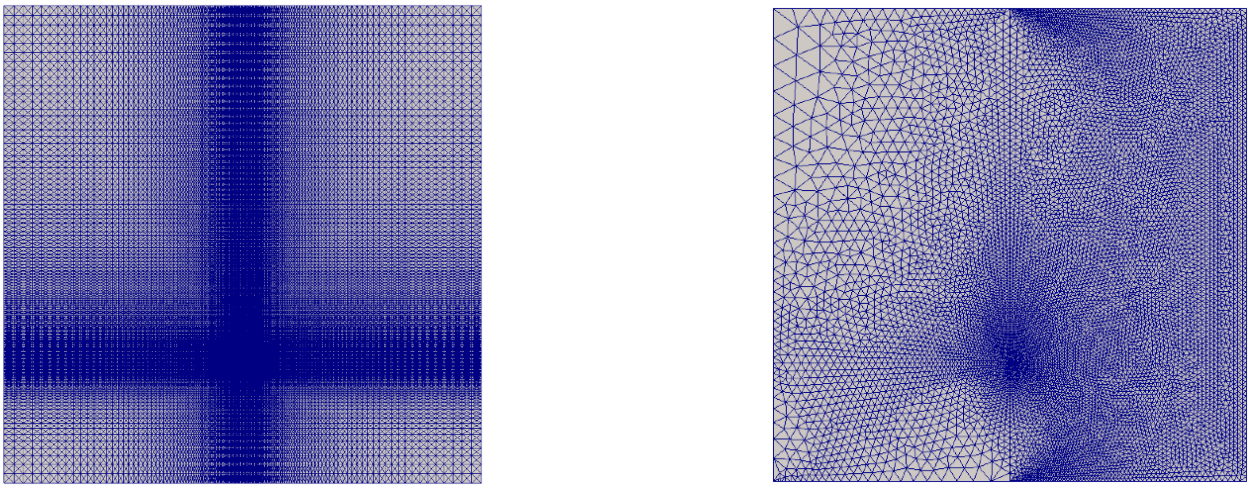

(a) **(b)**

Figure 6.12 Mesh designs with local refinement for **(a)** a structured mesh and **(b)** an unstructured mesh.

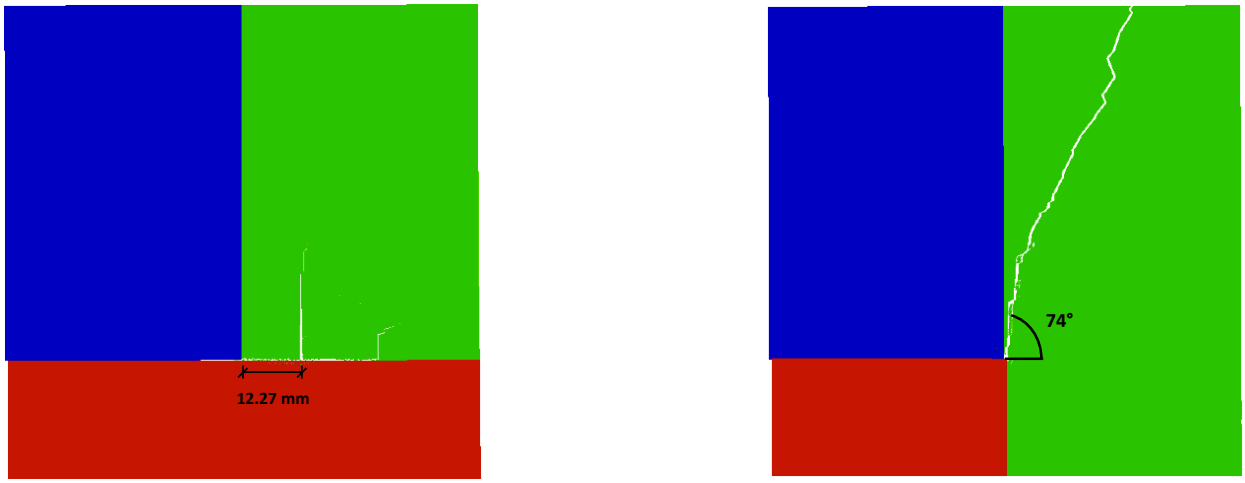

(a) **(b)**

Figure 6.13 Fracture path results for **(a)** the structured mesh with local refinement and **(b)** the unstructured mesh with local refinement.

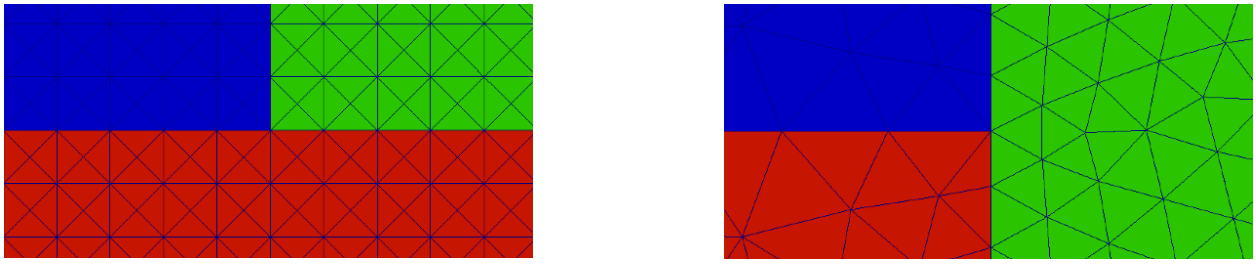

(a) **(b)**

Figure 6.14 Local refinement around notch tip (zoomed-in) for **(a)** structured mesh and **(b)** unstructured mesh.

The unstructured mesh above illustrates the effect of removing the horizontal edge. By eliminating the possibility for mode-II crack propagation along the horizontal edge, the unstructured mesh forced immediate transition to mode-I propagation, sending the crack tip along the 74° incline. Although this particular simulation using the DG method performed well compared to experimental and accepted research results, the other simulations employing the DG method all shared the delayed mode transition characteristic, predicting significant mode-II fracturing before transitioning to the inclined mode-I fracturing. Furthermore, the removal of the horizontal interface elements constitutes significant user input, which was to be avoided.

Another possible cause for the discrepancies between the simulations performed in this research and the simulations of Zhang [22], in particular, was the fact that linear elements were used. Zhang used quadratic T6 elements, where as these simulations used linear T3 elements. One reason the refined meshes were simulated was to obtain a more accurate representation of the process zone. Similarly, quadratic elements could provide a more accurate representation of this critical region as well, perhaps resulting in a crack path that more accurately represents experimental results and the results of other computational solutions to the problem. A new DG simulation was conducted using quadratic T6 elements on an 80x80 cross-quadrilateral mesh – the same setup as Zhang's simulation but using the DG method instead of the intrinsic cohesive zone method. The results are provided in Figure 6.15.

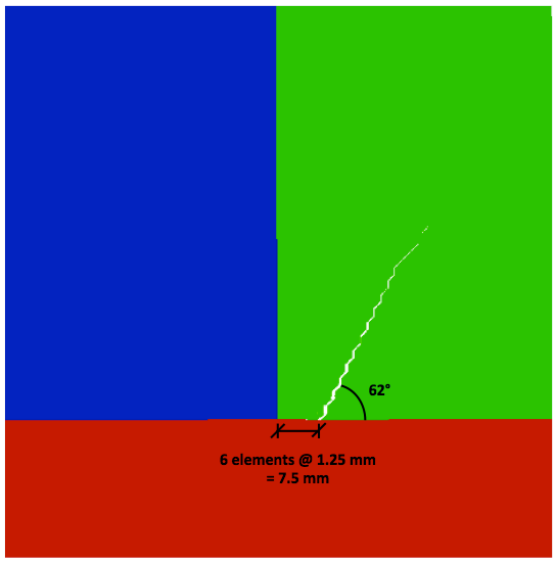

Figure 6.15 Fracture path for 80x80 cross-quadrilateral mesh of quadratic T6 elements.

Clearly the simulation failed to predict a crack initiating from the notch tip, but at 7.5 mm from the notch tip this simulation is the closest this research has come to the experimental observations. The propagation angle of 62° is reasonably close to the 70° experimental observation. The solution suggests that using quadratic elements does indeed provide a more accurate representation of the process zone, which according to experimental observations should promote mode-I brittle crack growth along the 70° direction.

7. CONCLUSIONS

Cohesive zone modeling can be an important tool for helping understand the mechanisms behind fracture and debonding. It can provide valuable insight into how and why structures fail. While intrinsic and extrinsic cohesive zone methods have proven useful, they come with disadvantages that make them particularly difficult to apply in dynamic simulations. Namely, the intrinsic methods bear the issue of artificial compliance wherein additional elastic potential energy is introduced to the system. Additionally, this method requires the specification of additional user-defined numerical tuning parameters like the initial slope on the traction-separation law. Extrinsic methods can become computationally expensive for large-scale problems due to the necessity of dynamically modifying the mesh topology and associated arrays when the failure criterion is met. The proposed Discontinuous Galerkin (DG) offers the ability to model fracture without the issues associated with traditional cohesive zone methods. The new contribution from this thesis is the application of the DG method to a mixed-mode dynamic problem for predicting arbitrary crack propagation – the Kalthoff-Winkler problem. This thesis primarily compared the performance of the proposed DG method to an intrinsic model and a hybrid DG/extrinsic model, as well as experimental observations. Many simulations of the KW problem were performed using the DG method in this thesis: structured and unstructured meshes of different textures and refinement, linear and quadratic elements, implicit and explicit integration schemes, and elastic and residual unloading constitutive models. A simulation was also conducted in Abaqus using native intrinsic cohesive interface elements.

All but one simulation resulted in a delayed mode transition, predicting significant mode-II fracturing before transitioning to the inclined mode-I fracturing, which does not agree with the experimental results or the results of other researchers' simulations of the problem. The only mesh that predicted a crack originating from the notch tip in this research did so because horizontal cohesive elements were not present at the notch tip. The simulations presented in this thesis predicted crack configurations that, while predicting the direction of the growth relatively accurately, did not accurately predict the location of initiation of the inclined crack. The focus of this thesis was directed to attempting to explain the discrepancies between the results predicted by the DG models and other numerical models and experimental data. Unfortunately, a definitive explanation was not determined. However, previous implementations of the DG method strongly suggest that it is a viable option for numerical modeling relative to other cohesive zone methods. The question still remains whether other modelers, such as Zhang and Nguyen, placed their cohesive elements along the horizontal edge emanating from the notch tip as was done in this research. The literature review revealed how sensitive the failure mode is to material properties, which also brings into question the reliability of experimental data from tests performed almost 30 years ago. While more recent experimental data has been reported on the shear-banding mode of failure, it appears little has been done experimentally in terms of the brittle mode of failure witnessed in the KW experiment.

Another contribution of this thesis was a novel technique for visualizing cohesive element data through wireframe figures. The technique produces illustrations for visualizing zero-thickness interface elements as thin lines, upon which cohesive element data can be conveyed with color contouring. This allows the interface elements to be studied independently

after a simulation is performed, and it provided valuable insights into the possible causes for the unexpected results encountered during this research.

The research presented in this thesis encourages future work. For example, the issue of delayed failure mode transition could be the result of the interpenetration of notch surfaces. In every simulation performed for this thesis, the faces of the original horizontal notch overlapped each other due to the absence of a finite gap in the numerical model and the presence of a negative mode-I stress intensity at the notch tip. In consideration of Lee and Freund's work [31], contact forces could be added to the surfaces on either side of the notch to prevent their overlapping. This more realistic model could encourage mode-I crack growth originating from the notch tip. Another option could be to prescribe a higher maximum shear stress than the tensile stress in order to facilitate mode-I cracking. However, the goal of the DG method remains to provide a robust technique capable of predicting natural material behavior with minimal user input.

REFERENCES

[1] Anderson T.L., Fracture mechanics: fundamentals and applications 3rd edition (2005).
[2] Griffith A.A., The phenomena of rupture and flow in solids. Phil Trans of the Royal Society of London 221 (1921) 163-198.
[3] Irwin G.R., Analysis of stresses and strains near the end of a crack traversing a plate. Trans ASME, J. Appl Mech 24 (1967) 361.
[4] Kalthoff, J., Modes of dynamic shear failure in solids. Int J of Fracture 101 (2000) 1-31.
[5] Ravi-Chandar, K., On the failure mode transitions in polycarbonate dynamic mixed-mode loading. Int J of Solids and Structures 32 (1995) 925–938.
[6] Truster T.J., Masud A., A discontinuous/continuous Galerkin method for modeling of interphase damage in fibrous composite systems. Comp Mech 52 (2013) 499-514.
[7] Kalthoff J.F., Winkler S., Failure mode transition at high rates of shear loading. Int Conf Impact Load Dynam Behav Mater 1 (1987).
[8] Cook R.D., Malkus D.S., Plesha M.E., Witt R.J., Concepts and applications of finite element analysis 4 (2002).
[9] Newmark N.M., A method of computation for structural dynamics. J Eng Mech 85 (1959) 67-94.
[10] Hughes T., The finite element method: linear static and dynamic finite element analysis (1987).
[11] Belytschko T., Chen H., Xu J., Zi G., Dynamic crack propagation based on loss of hyperbolicity and a new discontinuous enrichment. Int J Numer Eng 58 (2003) 1873-1905.
[12] Belytschko T., Tabbara M., Dynamic fracture using element-free galerkin methods. Int J Num Methods Eng 39 (1996) 923-938.
[13] Li S., Liu W.K., Rosakis A.J., Belytschko T., Hao W., Mesh-free galerkin simulations of dynamic shear band propagation and failure mode transition. Int J Solids Structures 39 (2002) 1213-1240.
[14] Klein P.A., Foulk J.W., Chen E.P., Wimmer S.A., Gao H.J., Physics-based modeling of brittle fracture: cohesive formulations and the application of meshfree methods. Theor and App Frac Mech 37 (2001) 99-166.
[15] Dugdale D.S., Yielding of steel sheets containing clits. J Mech Phys Solids 8 (1960).
[16] Barenblatt G.I., The mathematical theory of equilibrium cracks in brittle fracture. Adv Appl Mech 7 (1962).
[17] Seagraves, Radovitzky, Chapter 12 Advances in cohesive zone modeling of dynamic fracture (2010).
[18] Needleman A., A continuum model for void nucleation by inclusion debonding. J Appl Mech 54 (1987).
[19] Tvergaard V., Effect of fibre debonding in a whisker reinforced metal. Mat Sci and Eng 125 (1990) 203-213.
[20] Needleman A., An analysis of decohesion along an imperfect interface. Int J Frac 42 (1990) 21-40.
[21] Camacho GT, Ortiz M., Computational modeling of impact damage in brittle materials. Int J Solids Struct 33 (1996) 2899–2983.
[22] Zhang J.Z., Paulino G.H., Cohesive zone modeling of dynamic failure in homogeneous and functionally graded materials. Int J Plasticity 21 (2005).

[23] Nguyen V.P., Discontinuous Galerkin/extrinsic cohesive zone modeling: implementation caveats and applications in computational fracture mechanics. Eng Frac Mech 128 (2014).
[24] Lorentz E., A mixed interface finite element for cohesive zone models. Comp Meth in Appl Mech and Eng 198 (2008) 302-317.
[25] Truster T.J., Masud A., Primal interface formulation for coupling multiple PDE: A consistent derivation through the variational multiscale method. Comp Meth in Appl Mech and Eng 268 (2014) 194-224.
[26] Hicks W., Modeling of debonding and crack propagation in fibrous composites using a discontinuous galerkin approach. Unpublished Master's Thesis (2015). http://trace.tennessee.edu/utk_gradthes/3372/
[27] Truster T.J., Masud A., Discontinuous galerkin method for frictional interface dynamics. J of Eng Mech (2016).
[28] Talon C., Curnier A., A model of adhesion coupled to contact and friction. European J of Mech 22 (2003) 545-565.
[29] Truster T.J., On interface element insertion into three dimensional meshes. Eng. Fracture Mech 153 (2016) 171-174. http://clmi.utk.edu/software/
[30] Degarmo, E. P., Black, J. T., Kohser, R. A., Materials and processes in manufacturing 9 (2003) 119.
[31] Lee, Y. J., Freund, L. B., Fracture initiation due to asymmetric impact loading of an edge cracked plate. J Appl Mech 57 (1990).
[32] Mason J.J., Rosakis A.J., Ravichandran G., Full field measurements of the dynamic deformation field around a growing adiabatic shear band at the tip of a dynamically loaded crack or notch. J Mech Phys Solids 42 (1994) 1679-1697.
[33] Needleman A., Tvergaard V., Analysis of a brittle-ductile transition under dynamic shear loading. Int J Solids Structures 32 (1995) 2571-2590.
[34] Zhou, M., Rosakis, A. J. and Ravichandran, G., Dynamically propagating shear bands in prenotched plates: I--Experimental investigations of temperature signatures and propagation speed. J Mech Phys Solids 44 (1996a) 981-1006.
[35] Zhou M., Ravichandran G., Rosakis A.J., Dynamically propagating shear bands in prenotched plates: II--Finite element simulations. J Mech Phys Solids 44 (1996b) 1007-1032.
[36] Zhou M., Rosakis A.J., Ravichandran G., On the growth of shear bands and failure-mode transition in prenotched plates: a comparison of singly and doubly notched specimens. Int J Plast 14 (1998) 435-451.
[37] Belytshko T., Dolbow J., Nicolas M., A finite element method for crack growth without remeshing. Int J Num Meth Eng 46 (1999) 131-150.
[38] Park K., Paulino G.H., Celes W., Espinha R., Adaptive mesh refinement and coarsening for cohesive zone modeling of dynamic fracture. Int J Num Meth in Eng 92 (2012) 1-35.
[39] Park K., Paulino G.H., Roesler J.R., A unified potential-based cohesive model of mixed-mode fracture. J Mech Phys Solids 57 (2009) 891-908.

VITA

Russell Hollman was born in 1992 in Jackson, TN to Jim and Patsy Hollman. He is the oldest of three brothers: Luke, Alex, and himself. He attended the University School of Jackson in Jackson, TN for his high school education. After graduation, he began studying at the University of Tennessee in 2011, obtaining his B.S. in Civil Engineering in 2015. He then continued his education at the same university, obtaining his M.S. in Civil Engineering in 2017. In May 2016, he married his wife Holly, a Business Management Graduate from the Haslam College of Business at the University of Tennessee. While obtaining his M.S. degree, Russell worked as a graduate research and teaching assistant under Dr. Timothy Truster. His coursework includes: Reinforced Concrete Design, Steel Design, Masonry Design, Fiber Composites, Finite Element Applications in Structural Engineering, Structural Dynamics, and Structural Systems. Holly and Russell are now moving to Jacksonville, FL where he will begin his career as a structural consulting engineer.